Separation and transition on a cone-cylinder-flare: Experimental campaigns

Elizabeth Benitez, Matthew Borg, Sébastien Esquieu, Clément Caillaud, Mathieu Lugrin, Zachary McDaniel, Joseph Jewell, Anton Scholten, Pedro Paredes, Fei Li, et al.

Separation and Transition on a CCF: Experimental Campaigns

Elizabeth K. Benitez*
U.S. Air Force Research Laboratory, Wright-Patterson AFB, OH 45433

Clément Caillaud †
CEA-CESTA, 15 Avenue des Sablières, Le Barp, France

Zachary A. McDaniel‡
Purdue University, West Lafayette, IN, 47907

Mathieu Lugrin§
DAAA, ONERA, Université Paris Saclay, F-92190 Meudon - France

Sébastien Esquieu ¶
CEA-CESTA, 15 Avenue des Sablières, Le Barp, France

Matthew P. Borg‖
U.S. Air Force Research Laboratory, Wright-Patterson AFB, OH 45433

Joseph S. Jewell**
Purdue University, West Lafayette, IN, 47907

Anton Scholten††
North Carolina State University, Raleigh, NC, 27695

Pedro Paredes‡‡
National Institute of Aerospace, Hampton, VA 23666

Fei Li§§ and Meelan M. Choudhari¶¶
NASA Langley Research Center, Hampton, VA, 23681

Several experimental campaigns have been conducted across a number of Mach-6 facilities on the hypersonic flow around a CCF (CCF) geometry with a 5° half-angle cone and a 12° half-angle flare. These experiments were conducted as part of the NATO STO Research Task Group AVT-346, which is focused on predicting hypersonic boundary-layer transition on complex geometries. Two conventional wind tunnels (AFRL M6LT and ONERA R2Ch) and one quiet tunnel (Purdue BAM6QT) were used to test the same CCF geometry and to study the instabilities in both the boundary layer in the attached parts of the flow and the shear layer above the axisymmetric separation bubble near the cylinder-cone junction. Two nosetip radii (one nominally sharp and one blunt with a 5 mm radius) were tested. For the sharp nosetip case, there was a great deal of agreement between the measurements of both second-mode and shear-layer instabilities across the two conventional facilities. However, the measured

*Research Aerospace Engineer, Hypersonic Sciences Branch, elizabeth.benitez.2@us.af.mil, AIAA Member
†Research Engineer
‡Graduate Student, School of Aeronautics and Astronautics, AIAA Student Member
§Research Engineer
¶Research Engineer
‖Senior Aerospace Engineer, Hypersonic Sciences Branch, AIAA Associate Fellow
**John Bogdanoff Associate Professor, School of Aeronautics and Astronautics, AIAA Associate Fellow
††Graduate Student, Department of Mechanical and Aerospace Engineering, AIAA Student Member
‡‡Research Associate Fellow, Computational AeroSciences Branch, NASA LaRC, AIAA Associate Fellow
§§‡Research Scientist, Computational AeroSciences Branch
¶¶Senior Research Scientist, Computational AeroSciences Branch, AIAA Fellow

spectra for the blunt nosetip case showed more significant differences between the two tunnels, potentially due to an alternate dominant instability mechanism coupled with the variations in the freestream noise spectra. The quiet facility resulted in a flow that remained laminar to much higher freestream unit Reynolds numbers, as well as in instability measurements that had more distinct spectral peaks for the sharp tip case and broadband rises for the blunt one. The instability mechanisms at play in the sharp quiet case were found to be the same as those in the conventional facilities.

Nomenclature

f	=	frequency (kHz)
HLNSE	=	harmonic linearized Navier-Stokes equations
L_{sep}	=	bubble separation length (mm)
M	=	freestream Mach number
P	=	pressure (Pa)
PSD	=	power spectral density
Re_∞	=	unit freestream Reynolds number
Re_{tr}	=	Reynolds number at transition onset
Re_x	=	axial length Reynolds number
RMS	=	root mean square
SPOD	=	spectral proper orthogonal decomposition
T_0	=	stagnation temperature (K)
T_w	=	wall temperature (K)
U_∞	=	freestream streamwise velocity (m/s)
x	=	streamwise position (mm)
x_c	=	streamwise position relative to the cone-cylinder junction (mm)
Δ	=	change in quantity
μ	=	dynamic viscosity (kg/(m-s))
ρ	=	density (kg/m^3)
σ_{SPOD}	=	normalized SPOD modal energy

Facilities:

AFRL M6LT	=	Air Force Research Laboratory (AFRL) Mach-6 Ludwieg Tube
BAM6QT	=	Boeing/AFOSR Mach-6 Quiet Tunnel
ONERA R2Ch	=	ONERA Meudon R2Ch blowdown wind tunnel

I. Introduction

Reliable aerothermodynamic modeling for hypersonic vehicles is essential for designing vehicles that can withstand the harsh aerothermal environment experienced at high Mach numbers. One particular area of interest is shock-boundary layer interactions (SBLI), which happen in the vicinity of geometrical discontinuities (ramps, controls surfaces, etc.) and often significantly increase the local heat loads on the surface and impact the overall vehicle performance. The adverse pressure gradient due to the shock can cause the boundary layer to lift off the vehicle surface, creating a separation bubble. This interaction is complex because of the two-way coupling between flow separation and the state of the boundary, shear, and mixing layers, which makes it inherently difficult to study.

From the literature, three main features of separated hypersonic SBLI can be identified. Although there has been extensive research on hypersonic SBLIs over multiple decades, the first feature was unveiled by a study by Becker and Korycinski in 1956, whom were the first to focus on boundary layer transition in the presence of a separation bubble due to SBLI [1]. Their work focused on an ogive-cylinder-flare model and measured how trends in bubble geometry were impacted by the boundary-layer state, displaying the strong coupling between the separation region and the transitional dynamics. Then, the presence of striation in the reattachment region of SBLI was uncovered by Ginoux [2] who measured striations on the flare of a hollow cylinder-flare configuration. He also was the first to use the CCF

geometry in his experiments. One interesting point in this study is that the striation became less apparent upon the addition of the conical forebody. These streamwise striations have been the subject of several later studies seeking to understand their origin and role in transition [3–6]. Then, the last feature is temporal unsteadiness related to laminar or transitional SBLIs, which was first measured in the 1980s [7, 8]. Recent work has focused on measuring a shear-layer instability that manifests as a travelling wave in the shear-layer and the reattached boundary layer. Such an instability was measured on the Oberkampf and Aeschliman geometry [9] when artificial plasma perturbation was used to provide a large, controlled initial disturbance [10]. It was observed naturally with a CCF by Benitez et al. [11] in 2020 and a hollow cylinder-flare geometry by Lugrin et al. [12] in 2022 . Similar waves were also noted by Butler and Laurence [13] over a sharp cone-flare geometry shortly afterward.

The particular geometry for the series of experiments described in this article was originally designed by Esquieu to generate an axisymmetric separation under hypersonic flow [14, 15]. A 10° half-angle flare version of the geometry, henceforth referred to as the 10° flare, was extensively studied under quiet flow [11, 16–18], where both the second mode and a shear-layer instability were identified. While instability amplification was observed downstream of reattachment, no turbulent spots were naturally generated in the low-disturbance environment. Computational analysis in 2021 revealed that a slightly larger, 12° half-angle flare, henceforth referred to as the 12° flare, might provide sufficient instability to cause transition onset [19]. That geometry was used during the present work.

This paper describes the compiled experimental findings from the separation-bubble instability and transition subtask under NATO AVT-346 (Predicting Hypersonic Boundary-Layer Transition on Complex Geometries). These experimental campaigns were focused on the CCF geometry at zero degrees angle of incidence, which leads to an axisymmetric separation bubble. Experiments took place across three unique facilities: the AFRL Mach-6 Ludwieg Tube at AFRL, the ONERA R2Ch facility in Meudon, and the Boeing/AFOSR Mach-6 Quiet Tunnel at Purdue University. There is also a companion paper focused on the computational side of this study [20].

The paper begins with a summary of previous experimental work on the CCF geometry, followed by a description of the experimental setup used for the current study. The effect of varying freestream unit Reynolds number at the M6LT and R2Ch facilities is then explored. Afterward, two specific run conditions (one for each nosetip radius) are selected for more detailed study from the conventional tunnels. Finally, the experimental results under quiet flow from the BAM6QT are presented.

II. Summary of Prior CCF Experimental Results

Initial testing involved the 5°/3.5° CCF model, i.e., , 5° half-angle cone - cylinder - 3.5° half-angle flare, and sharp nosetip to study the impact of axisymmetric compression without a separation bubble [14, 15, 21]. This geometry was tested under both quiet flow and conventional noise at the BAM6QT using IR thermography and PCB pressure fluctuation sensors. Computations were also performed with STABL2D. The second (Mack) mode was measured in the pressure fluctuations along the cone, cylinder, and flare section. Instability amplification was noted along the cone and flare, while the second mode was damped along the cylinder. Excellent agreement was found between the computational results for both the heat transfer, as well as the second-mode peak frequencies and growth rates along the flare (Figure 1).

Extensive measurements were made for the CCF model with a 10° half-angle flare and sharp nosetip [21]. Initial testing at 0.0° angle of attack under quiet flow revealed naturally amplified shear-layer waves in both the shear layer near reattachment and the reattached boundary layer (Figure 2) [11]. Both instabilities consisted of travelling waves that convected downstream in the shear layer and reattached boundary layer. The second mode was considered neutrally stable in the shear layer, but started amplifying again near reattachment. The shear-layer instability, however, appeared neutrally stable downstream of reattachment. At a given streamwise location, increasing the freestream unit Reynolds number caused the second mode power spectral density (PSD) peaks to increase in both amplitude and frequency, while the shear-layer instability peaks increased in amplitude with a constant peak frequency. Holding freestream unit Reynolds number constant and moving downstream resulted in the second mode amplifying while maintaining a constant peak frequency, while the shear-layer instability was relatively stable in amplitude but generally increased in peak frequency [11]. For all freestream unit Reynolds numbers tested, the boundary layer remained laminar to the downstream edge of the model, with no turbulent spots observed. As the unit Reynolds number increased, the reattachment point for the separation moved downstream, consistent with the expectation for a laminar bubble [1].

Small variations in the angle of attack were made on the 5°/10° CCF, i.e., 5° half-angle cone - cylinder - 10° half-angle flare, to observe the effect of small nonzero angles of attack on bubble geometry and boundary-layer instability [16]. Under quiet, laminar flow, increasing the angle of attack resulted in reattachment on the windward side moving upstream. This change created a smaller bubble locally and a longer region downstream of reattachment. No turbulent

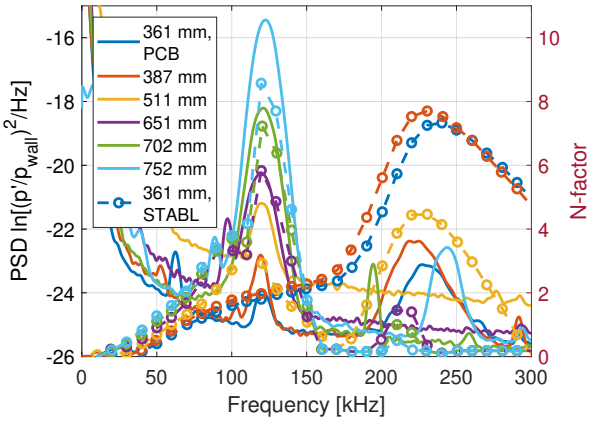

Fig. 1 BAM6QT experimental surface pressure fluctuation PSDs and computed N-factors for multiple locations along the 5°/3.5° CCF. $Re_\infty = 11.2 \times 10^6$/m. Solid lines are PCB measurements while dashed lines are computed from STABL. Replotted from Ref. [21].

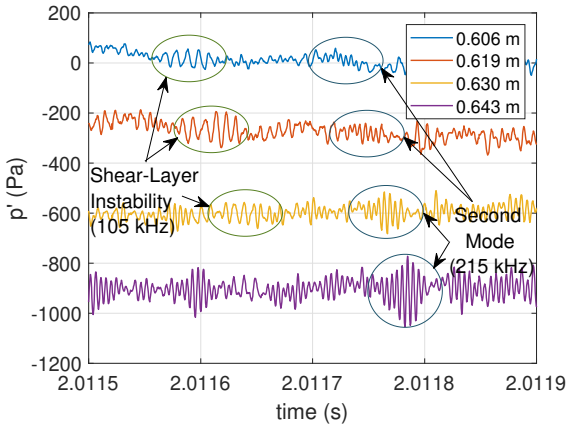

(a) Time series for $Re_\infty = 12.0 \times 10^6$/m.

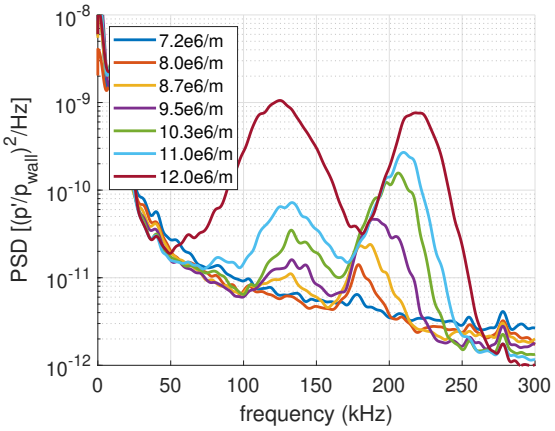

(b) PCB power spectral densities at 0.630 m from the nosetip

Fig. 2 Time series and PSD plots showing the shear-layer instability (between 100-150 kHz) and the second mode (between 170-250 kHz) in pressure fluctuations under the reattached boundary layer. Data is zero-centered but offset for clarity. Reprinted from Ref.[18].

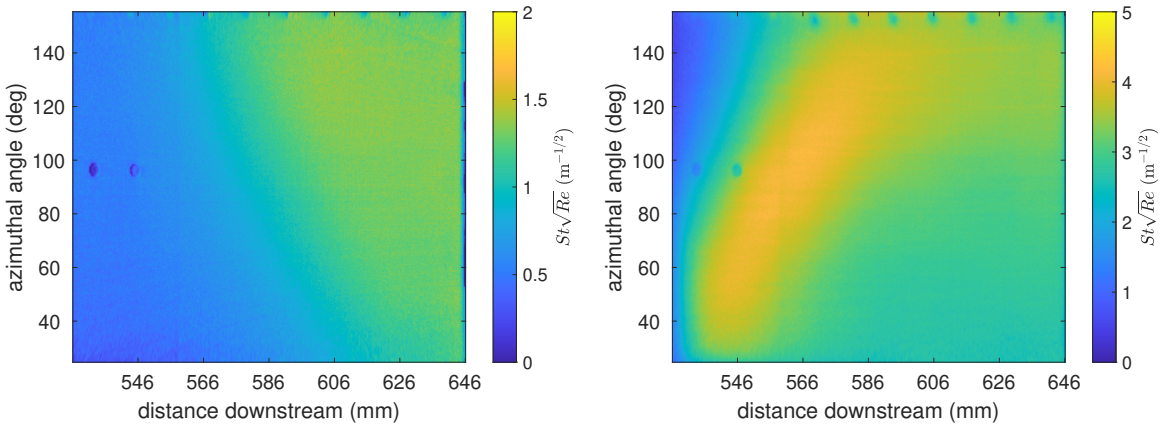

(a) Quiet, laminar flow. $Re = 11.5 \times 10^6$**/m.** **(b) Conventional noise, transitional flow.** $Re = 6.05 \times 10^6$**/m.**

Fig. 3 Heat flux (in scaled Stanton number) for the 10° flare at 0.6° angle of attack. The windward side is at an azimuthal angle of 180°. Note the opposing trends in reattachment position for the quiet, laminar flow compared to the conventional noise, transitional flow. Reprinted from Ref. [16].

spots were measured at any of the small angles of attack tested. Under conventional noise, the flow was transitional. For this case, increasing the angle of attack resulted in reattachment on the windward side moving downstream. Figure 3 plots the 10° flare heat-flux profile for the largest angle of attack tested (0.6°), highlighting the inverse trend in bubble geometry between the quiet, laminar cases and the conventional noise, transitional ones.

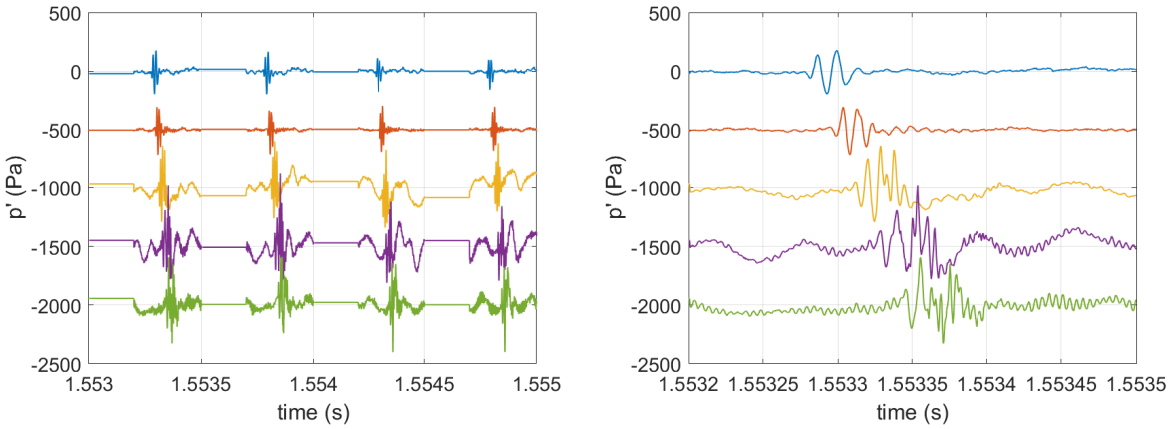

(a) Four consecutive induced wave packets. **(b) Enhanced view of single wave packet.**

Fig. 4 Wave packets in the reattached boundary layer resulting from plasma perturbation with a 12.5 kV controlled disturbance. $Re_\infty = 11.6 \times 10^6$**/m, reprinted from Ref. [18].**

To attempt to measure turbulent spots under quiet flow, a plasma perturber was integrated into the 5°/10° CCF model to input short, high-amplitude, disturbances into the boundary layer upstream of the separation bubble [17]. By installing the perturber electrodes at the downstream end of the cone, the artificial disturbance could convect through the shear layer and result in a larger fluctuation for the frequencies that are naturally amplified in that region. Some sample surface pressure wave packets, measured in the reattached boundary layer, resulting from the perturbation are plotted in Figure 4 [18]. The artificial disturbances resulted in amplified waves within the band of the shear-layer instability (80–120 kHz), which continued to amplify in the reattached boundary layer before breaking down into turbulent-spot-like packets.

The 5°/12° CCF model, i.e., 5° half-angle cone - cylinder - 12° half-angle flare, was designed based on global

instability calculations that suggested the slightly larger angle may be sufficient to trigger transition onset under quiet flow [22]. This flare angle was initially tested at the AFRL M6LT with the two blunter nose tips under conventional noise [23]. Those tests resulted in a transitional separation bubble with reattachment points that generally moved upstream with increasing freestream unit Reynolds number. The instability spectra were more ambiguous than the quiet-flow results, with potential peaks around 25 and 60 kHz observed in the PCB PSDs as well as the SPOD analysis. Initial tests were also run in the BAM6QT under quiet flow, which resulted in naturally-generated turbulent spots observed breaking downs from shear-layer-instability wave packets [24, 25].

This paper presents new results from the R2Ch facility, the AFRL M6LT, and the BAM6QT for measurements of the 5°/12° CCF.

III. Experimental Setup

A. Hypersonic Test Facilities

The same geometry was tested at three different hypersonic facilities across the United States and France to provide similar measurements made under different freestream noise conditions. Specifically, two models were fabricated to have the same outer mold line. This cross-facility comparison provides insight into receptivity effects and can promote understanding of the impacts of tunnel-specific parameters such as varying stagnation temperature.

1. Air Force Research Laboratory Mach-6 Ludwieg Tube (AFRL M6LT)

The AFRL Mach-6 Ludwieg Tube is located at the Air Force Research Laboratory (AFRL) in the state of Ohio. This facility is a low-enthalpy conventional hypersonic tunnel with the ability to rapidly conduct runs at a variety of freestream unit Reynolds numbers. The prerun stagnation temperature is maintained at around 505 K using a heated driver tube. Each run is actuated by a fast valve located upstream of the nozzle, allowing for minimal time between runs. The tunnel has optical access of the test section via 12-inch (304.8 mm) windows on either side for schlieren, FLDI, or other optical techniques, as well as a smaller window above for simultaneous IR. An illustration of the AFRL M6LT is shown in Fig. 5.

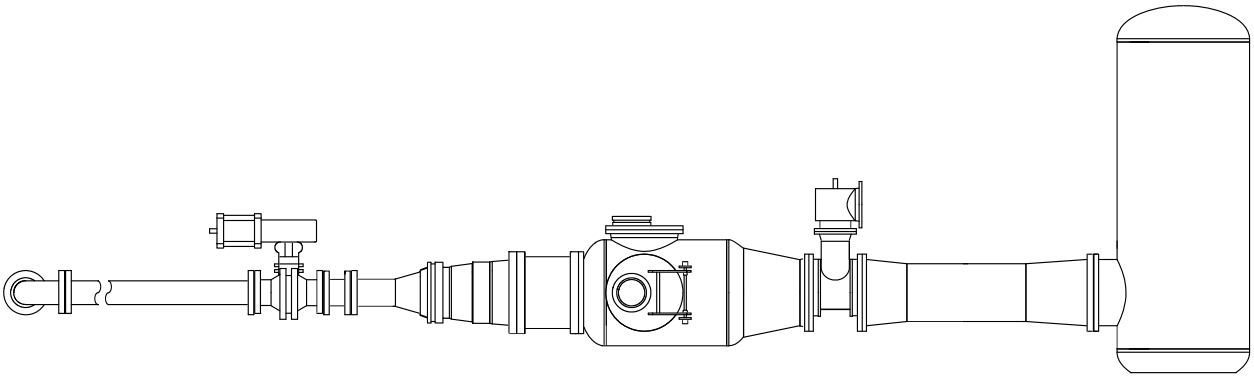

Fig. 5 AFRL M6LT schematic.

The AFRL Ludwieg Tube is capable of running with stagnation pressures between 0.35×10^6 Pa and 4.00×10^6 Pa, corresponding to unit Reynolds numbers between 2.3×10^6/m and 30.1×10^6/m. A single run includes two 100 ms periods of quasistatic Mach-6 flow before the tunnel unstarts. While not a quiet tunnel, freestream noise has been consistently measured by the percent RMS pitot fluctuations to be below 3% of the initial driver pressure. The flow during a run is at Mach 6.1. For more detailed information about the operating conditions of this tunnel, see Kimmel et al. [26].

2. ONERA R2Ch

The R2Ch facility is located at the ONERA Meudon site in France. It is a low-enthalpy conventional blow-down wind tunnel. A set of contoured axisymmetric nozzles with an exit diameter of 327 mm produces Mach 5, 6 and 7 flows. The air supply and pressure regulation stage produces dry air with stagnation pressure up to 8×10^6 Pa and run times at

constant conditions of up to a minute (albeit runs of 10 to 30s were used in the present study) thanks to a 500 cubic meter vacuum sphere. An accumulation Joule-effect heater preheats the compressed air to a stagnation temperature of up to 750 K. The free-stream static pressure fluctuations of R2Ch have been measured to be less than 2% for the Reynolds number considered in this study.

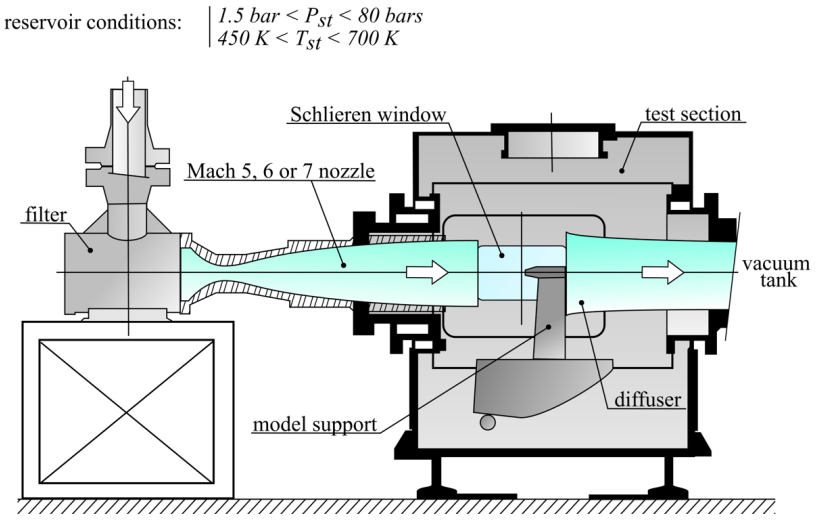

Fig. 6 R2Ch schematic.

3. Boeing/AFOSR Mach-6 Quiet Tunnel (BAM6QT)

The Boeing/AFOSR Mach 6 Quiet Tunnel (BAM6QT) is located at Purdue University in the state of Indiana. The BAM6QT is a Ludwieg tube that is capable of running with conventional noise or quiet flow with run times of up to 6 seconds. The test section is located in the downstream end of the diverging section of the nozzle and includes optical access with a variety of windows. A diagram of the tunnel can be found in Fig. 7.

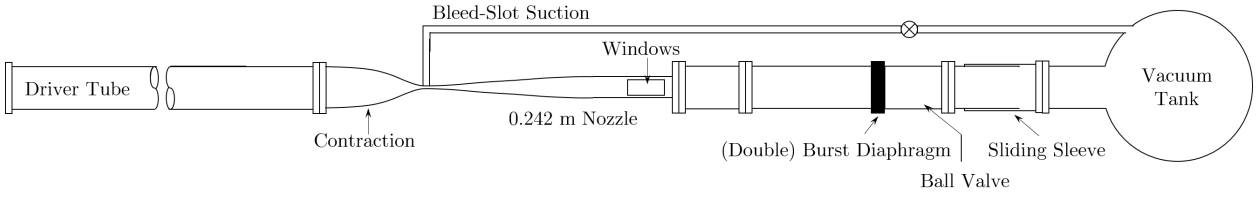

Fig. 7 BAM6QT schematic.

The BAM6QT consists of a 37.3 meter driver tube connected to a nozzle with a converging-diverging design, which exhausts into a 113 cubic meter vacuum tank. To avoid condensation, the air is heated and dried. The tunnel is equipped with a diaphragm system located downstream of the test section, consisting of two thin aluminum sheets separated by an air gap; the air in this gap is evacuated to start a run. During the time between reflections, steady Mach 5.8 or 6.0 flow (depending on the run noise level) is achieved for approximately 200 ms. By obtaining data during different stages of this reflection cycle, a range of unit Reynolds numbers can be measured in a single run.

To obtain quiet flow, a combination of several features are implemented to reduce disturbances and keep the boundary layer on the nozzle laminar, including a polished nozzle, particle filter, and bleed slots at the throat. Together, these features allow the tunnel to operate with very low freestream noise levels (less than 0.02%) [27]. However, at high enough unit Reynolds numbers the flow will still be noisy. Since a turbulent boundary layer along the diverging portion of the nozzle is thicker than a laminar one, the effective diameter of that part of the nozzle is smaller. This results in Mach 5.8 flow, as opposed to the Mach 6.0 achieved during a quiet run.

B. Models

1. BAM6QT and AFRL M6LT Model

The same model was used at both the BAM6QT and the AFRL M6LT. The separating axisymmetric compression corner model consists of a CCF geometry originally designed by Esquieu [14, 15]. It is divided into three components, with a stainless steel nosetip, aluminum cone-cylinder (with a 5° half-angle for the cone), and PEEK cylinder-flare (12° half-angle conical flare). In addition to a sharp (radius of 0.1 mm) nosetip, two blunt nosetips were tested (radii of 1 mm and 5 mm, respectively).

Figure 8 shows a drawing of this model. There are ports for up to 18 PCB sensors, with 15 along the central sensor ray (azimuthal angle of 180°) and 3 located azimuthal angles of 0°, 90°, and 270° along the cone for alignment purposes. Additionally, there are 27 ports for Kulite® sensors, with 12 located 30° from the main ray. The remaining 15 ports are divided into three groups of 5 sensors each that span the azimuth between the PCB and Kulite® rays (between 180° and 210°). These sensors are separated by 5° azimuthally and by 1 inch in the streamwise direction.

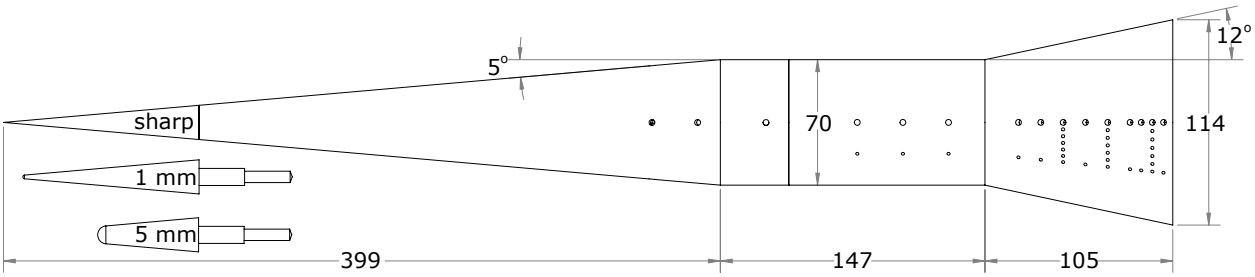

Fig. 8 5°/12° CCF model used in the BAMQT/AFRL experiments. All three nose tips (sharp, 1 mm, and 5 mm radius) were tested. Dimensions in millimeters.

The yaw and angle of attack for the model was zeroed using four PCB sensors located 90° apart azimuthally at the same downstream location along the 5° cone. The second-mode peak frequency was determined at each of these sensors. When at 0.0°, the peak frequencies from all four sensors should theoretically be the same. In practice, the model was adjusted until the four peaks were within 4% of the mean peak frequency.

For this set of experiments, all three nosetips were used. PCB stations along the flare were primarily used for measuring the surface pressure fluctuations, although some Kulite® measurements were also taken in previous entries.

2. ONERA and CEA Model

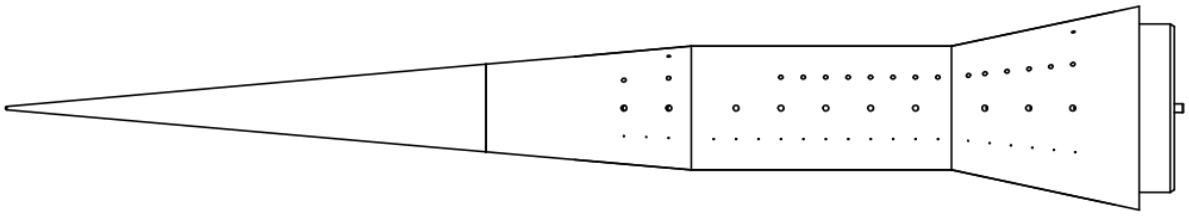

Fig. 9 12° CCF model from CEA used in the experiments at R2Ch, three different nosetips can be used (sharp, 1 mm, and 5 mm radius). The dimensions are the same as the BAM6QT and AFRL M6LT model. Small, medium and big holes correspond to pressure taps, Kulite® sensors and PCB sensors respectively.

The R2Ch model uses the exact same geometry as the BAM6QT and AFRL model, but the sensor layout is different as observed in Fig. 9. The model is equipped with 10 PCB, 18 Kulite® sensors and 23 pressure taps. The yaw and angle of attack for the model was zeroed ($\alpha < 0.12°$) using four static pressure taps. While three nosetips with the same radii as the BAM6QT and AFRL model were constructed, only the sharp and 5 mm nosetip were used in the experiments.

C. Instrumentation

1. Surface Pressure Sensors

Surface pressure-fluctuation measurements were acquired with PCB132B38 sensors as well as Kulite® XCE-062-15A and 5A sensors during most of the experimental campaigns. For the R2Ch campaign, two TE Connectivity 16MS pressure scanners were used for the pressure taps.

The PCB sensors, manufactured by PCB Piezotronics, are high-pass filtered above 11 kHz and have a high-frequency response limit of 1 MHz, albeit resonance of the sensor have been observed for frequencies as low as 300 kHz. Their nominal resolution of 6.89 Pa coupled with a rise time of less than 3 μs provides a voltage, which can be scaled using the factory calibration to obtain pressure measurements. PCB132B38 sensors have a surface diameter of 3.2 mm.

Kulite® XCE-062-15A and 5A sensors were used to acquire lower-frequency disturbances and static pressures. These transducers are smaller than PCBs, with a 1.7 mm diameter, but have a slower response time. This lower response time, coupled with a large resonance peak, restrict their useful output to below 270 kHz. The sensors were calibrated by manually changing the test section pressure and recording voltages across a known range.

At the AFRL M6LT, the PCB data were sampled at 20 MHz with an HBM data acquisition system, and low-pass filtered at 5 MHz. At R2Ch, the PCB were conditioned using 4-channel PCB 482C05 signal conditioners with no amplification nor filtering. The signal is then digitized by two NI PXIe-6376 cards with a sampling frequency set to 3.3 MHz. The PCB are flush mounted with an epoxy cap using the technique described in Ref. [12]. At the BAM6QT, data taken with the PCB sensors were sampled at 5 MHz with an HBM data acquisition system, and analog low-pass filtered at 1.25 MHz to preclude aliasing.

2. High-Speed Schlieren Imaging

High-speed schlieren imagery was captured during the experimental campaigns at all three experimental facilities. It was used to both visualize the average bubble geometry and study the instabilities along the shear layer and reattached boundary layer via SPOD analysis [28].

At the AFRL M6LT, a Photron Fastcam SA-Z-2100K-M-32GB high-speed camera captured the images from a self-aligned focusing schlieren (SAFS) apparatus. The SAFS setup was used to reduce the line-of-sight integration experience by Z-type schlieren. The depth of focus was adjusted to exclude the turbulent shear layers that emanate from the nozzle exit. Lighting was provided by a Cavitar Cavilux HF 640 nm laser, with pulse lengths set at either 90 and 150 ns depending on the frame rate. Images were taken at frame rates of 20 or 210 kHz, with higher frame rates limited by reduced viewing windows. The lower-framerate runs were time-averaged to measure the estimated bubble reattachment point. Spectral proper orthogonal decomposition (SPOD) was used to analyze the high-framerate cases to better visualize any present instabilities [28]. This allows us to get a mathematically optimal decomposition of spatiotemporally correlated structures present in the images.

At ONERA R2Ch, high-speed schlieren was conducted using a Phantom TMX-7510 camera using a folded Z-type schlieren apparatus. The lighting was provided by a continuous 300 Watt xenon source, the camera providing sufficiently low exposure time (200ns) to avoid motion blur. The images were sampled up to 875 kHz for the maximum duration allowed by camera memory (around 2 seconds).

At the BAM6QT, a Phantom TMX 7510 high-speed camera was also used to capture the images from a Z-type schlieren apparatus with 8-inch parabolic mirrors. Lighting was provided by a Cavilux SMART high-speed illumination system with pulse lengths set to 10 ns. Images were taken at frame rates of either 95 or 875 kHz, with higher frame rates only collecting a discrete number of image bursts while the 95-kHz rate was capable of obtaining images of the duration of the run.

The high-speed schlieren from each tunnel was used to conduct an SPOD analysis [28, 29]. SPOD extracts spatialtemporally coherent structures from the schlieren images, allowing for the extraction of peak frequencies associated with coherent mode shapes. However, the method is sensitive to several experimental parameters, such as frame rate and the total number of frames. A large number of frames at a frame rate higher than the Nyquist frequency (twice the maximum measurable frequency) is necessary to resolve fluctuations in the SPOD modal energy. Table 1 summarizes the SPOD parameters used at each of the facilities for this study.

3. Diagnostics Summary

A summary of the diagnostics utilized at each facility for this particular study is provided in Table 2.

Table 1 SPOD parameters for each facility.

	AFRL M6LT	ONERA R2Ch	Purdue BAM6QT
# Blocks	139	800	110
# Snapshots/Block	210	1024	200
Block Overlap	105	0	55

Table 2 Diagnostic summary for each facility.

	AFRL M6LT	ONERA R2Ch	Purdue BAM6QT
PCB132B38	20 MHz sampling rate	3.3 MHz sampling rate	5 MHz sampling rate
Kulite®	NA	1.1 MHz sampling rate	NA
Pressure Taps	NA	100Hz sampling rate	NA
Schlieren Camera	Photron Fastcam SA-Z	Phantom TMX-7510	Phantom TMX-7510
Schlieren Frame Rate	$\leq$ 210 kHz	$\leq$ 875 kHz	$\leq$ 1.7 MHz
Schlieren Light Source	Cavilux HF	Xenon source	Cavilux SMART
Schlieren Light Pulse Length	$\leq$ 150 ns	continuous (200 ns exposure time)	10 ns
Schlieren Setup	SAFS	Z-type	Z-type

D. Computational Methods

A subset of run conditions have been replicated computationally and select results are included to compare with the experiments. For more detailed computational results and a full explanation of the numerical methodology, see the companion paper focused on the numerical study [20].

IV. Reynolds Number Effects

A. Experimental Run Conditions Comparison

In order to give an overview of the tunnel entries discussed in the following sections, Figure 10 plots the stagnation temperatures and pressures during each run from the AFRL M6LT and the R2Ch tunnels. The AFRL facility utilizes a constant stagnation pressure of 505 K prior to each run, so has little variation in T_i across runs; the freestream unit Reynolds number is set by the initial stagnation pressure in the driver tube. At the R2Ch facility, however, the maximal initial stagnation temperature scales with the stagnation pressure, resulting in a larger range of T_i values.

Figure 11 plots the estimated separation and reattachment points for the AFRL M6LT and R2Ch facility runs for the sharp and 5 mm nosetips. Reattachment point estimates were also included for the BAM6QT, which did not have the instrumentation to determine separation point or overall bubble length. The positions were found using two different methods due to the different instrumentation options from the two tunnels. For the AFRL M6LT, the time-averaged schlieren was used, with the separation point determined by finding the intersection of the separation shock with the boundary layer along the cylinder. The reattachment point (for both AFRL and the BAM6QT), however, was estimated by fitting a trendline along the reattached boundary layer on the flare, and finding the location where the boundary layer began to curve away from it. This method is similar to what has been previously employed by Butler and Laurence [13] and Benitez et al. [25], with the latter showing excellent agreement to computations for a fully laminar bubble. For the R2Ch data, the 20 static pressure taps along the model were instead used to estimate the separation and reattachment points. The separation location was determined based on the position where the static pressure along the cylinder departs from the free-stream value, while the reattachment location was determined when a positive steepening of the pressure profile on the flare after the pressure plateau in the separation bubble was detected.

As the freestream unit Reynolds number increased for the sharp-nose cases from both tunnels, the separation point shifted downstream while the reattachment point shifted upstream, resulting in a smaller bubble at higher Re_∞. This trend is expected for transitional flow [1] and is believed to be due to a retroaction of the transition at reattachment on the mean separated region [5]. Similar behavior has also been reported for incompressible separated regions [30].

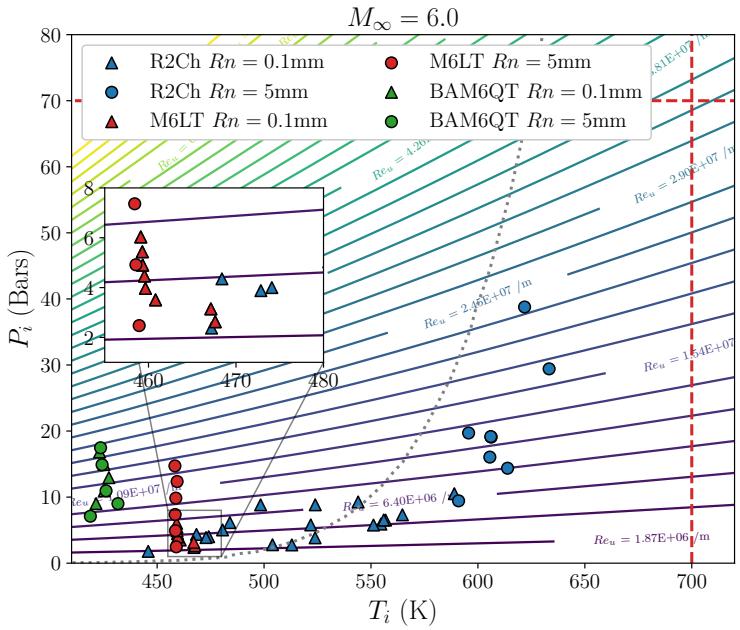

Fig. 10 Overview of the wind tunnel runs considered in (T_i, P_i) space with Reynolds numbers in contour lines. M6LT runs are colored in red and R2Ch runs are colored in blue. Sharp and blunt nosetips are, respectively, identified with triangle and round markers.

The transitional behavior of the flow is confirmed by the turbulent surface pressure spectra measured by pressure transducers on the flare (see Figure 14). The separation points agreed well across facilities, and was generally within 15 mm at a given Reynolds number. The reattachment point varied slightly as well, and seemed to occur also about 15 mm upstream at R2Ch relative to the AFRL M6LT. It is possible that the separation and reattachment location discrepancy is due to the different methodologies used to obtain the estimated reattachment position. However, when the bubble separation lengths are plotted as a function of Re_∞ (see Figure 11b), they are nearly identical between the two facilities.

A different trend was observed for the blunt, 5 mm nosetip cases. At both facilities, as Re_∞ increased from the lowest value out to about 6×10^6/m, the separation point shifted upstream while the reattachment point shifted downstream, resulting in a larger bubble at higher Re_∞. This trend is expected for laminar flow [1], which again agrees with the surface pressure spectra (see Figure 17). In this Reynolds number range, the separation location agreed very well across both facilities, while the reattachment point was nearly 50 mm farther downstream at AFRL than R2Ch, possibly due to the different estimation methodologies again. Above $Re_\infty = 6 \times 10^6$/m, the bubble size remains relatively stable from the AFRL data, while it began to decrease in size from the R2Ch data. This is due to the fact that the flow becomes transitional in R2Ch while it remains laminar at AFRL.

B. Sharp Nosetip

Initial analysis was conducted for the sharp nosetip configuration. With this tip, under conventional freestream noise levels, the flow was generally laminar with strongly amplified instabilities along the cylinder-flare section, with breakdown happening near the reattachment point. As mentioned previously, the bubble size tended to decrease with increasing freestream unit Reynolds number. Figures 12 and 13 show some time-averaged schlieren images of the cylinder-flare junction from the AFRL M6LT and R2Ch, respectively. The horizontal axis displays distance from the cone-cylinder junction while the vertical one shows height off the cylinder; both axes are in millimeters. The AFRL images were created by combining three independent runs that had different viewing areas but the same freestream conditions, with the viewing frame edges smoothly averaged to create the final image, while the R2Ch images are each from an individual run. From both facilities, as Re_∞ increased, the separation point shifted downstream while the reattachment point shifted upstream.

Surface pressure power spectral densities (PSDs) were obtained along each of the three sections of the model at a range of freestream unit Reynolds numbers and are presented in Figure 14. The solid lines are wall pressure fluctuation

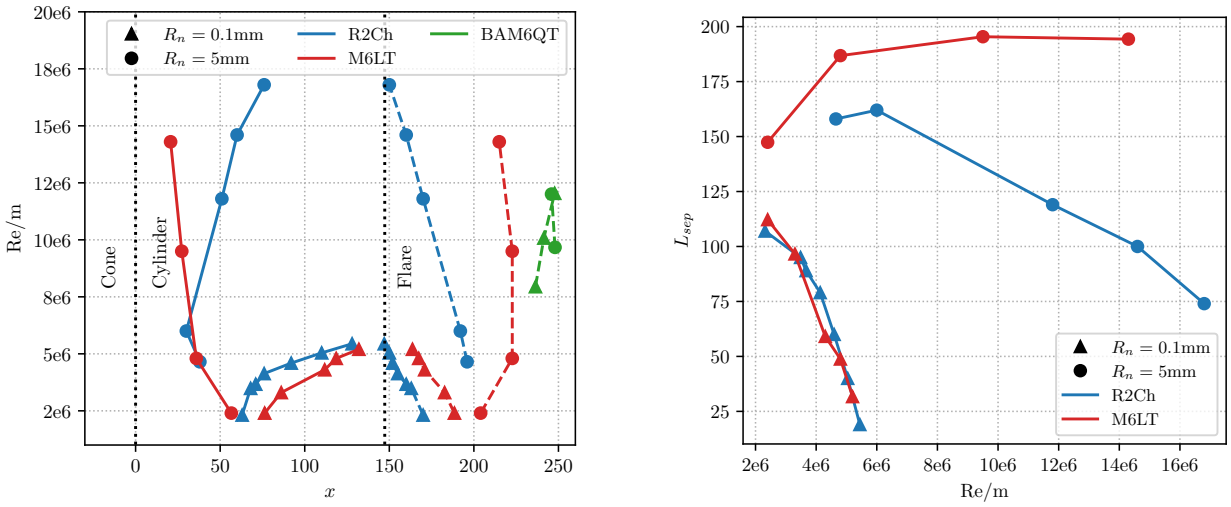

(a) Separation and reattachment position. **(b) Bubble lengths**

Fig. 11 Summary of the bubble size trends on sharp and blunt models, across Reynolds numbers for M6LT and R2Ch facilities. BAM6QT data were only available for the reattachment point estimation.

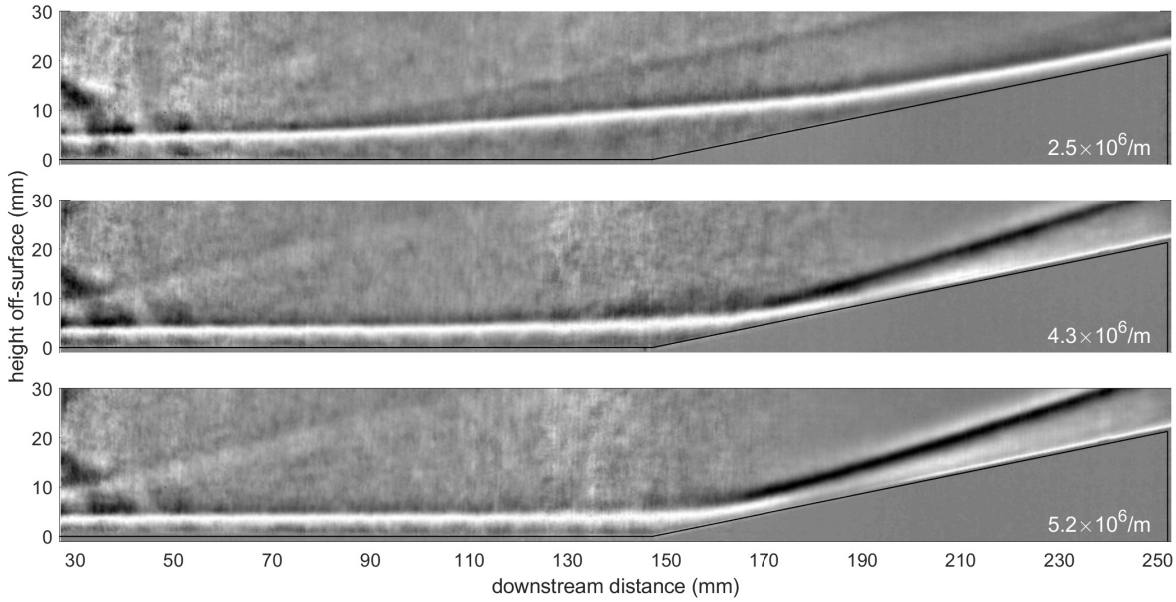

Fig. 12 Sharp nosetip time-averaged and concatenated schlieren imagery from the AFRL M6LT, for $Re_\infty = 2.5 \times 10^6$/m, 4.3×10^6/m, and 5.2×10^6/m.

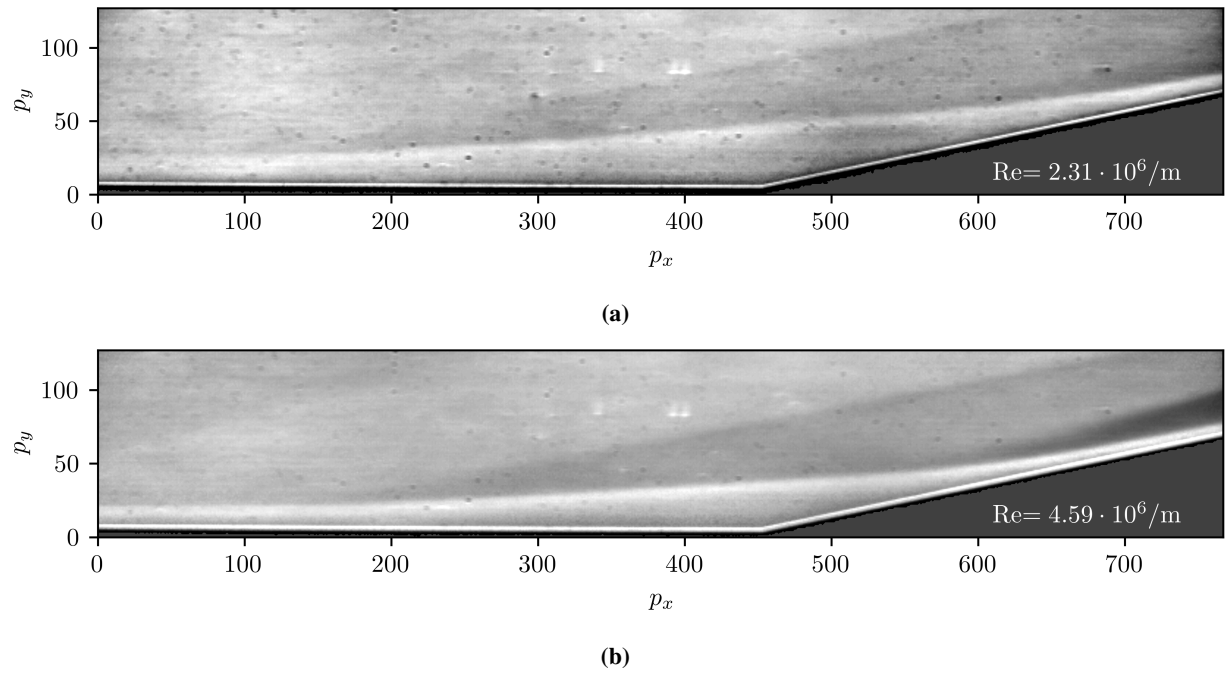

Fig. 13 Sharp nosetip time-averaged schlieren imagery from the R2Ch, for $Re_\infty = 2.31 \times 10^6$/m and 4.59×10^6/m.

PSDs during the run, while the semitransparent lines represent the prerun noise. Along the cone, clear second Mack mode peaks are visible between 100 and 200 kHz for both the AFRL M6LT and the R2Ch facilities. Excellent agreement is seen in both peak frequency and normalized amplitude from both tunnels. Note that the irregular spacing of the R2Ch spectral peaks is due to the inconsistency of the stagnation temperature at that facility; the M6LT peaks display a more regular spacing due to greater control of T_0. The peak shifts toward high frequency with increasing freestream unit Reynolds number, as the boundary layer becomes thinner. It also increases in amplitude until about $Re_\infty = 5 \times 10^6$/m, where nonlinear saturation limits the increase in amplitude. The presence of nonlinearity is confirmed by the spectra for the AFRL data, where most Reynolds numbers clearly display a harmonic at twice the peak frequency of the second mode. The R2Ch results also have a harmonic for a subset of the runs, but the data are more obscured by the noise floor and the resonance of the sensor.

Along the cylinder, for both facilities, going through the expansion fan strongly decreases the second mode amplitude. Then, along the cylinder, the second mode decreases in peak frequency with the thickening of the boundary layer. Once again, good agreement is observed in both the peak frequencies (generally between 30 and 100 kHz) and amplitudes in the PSDs. However, the AFRL PSDs also began developing a lower-frequency peak between 10 and 20 kHz that is not apparent in the R2Ch results. These peaks, like the second mode, increase in peak frequency with increasing Re_∞. The additional peaks may be the result of a different freestream noise environment (discussed further in Section IV.C).

Along the flare, near or downstream of reattachment, the spectra were mostly broadband at the higher Re_∞ values for both facilities, indicating a transition to turbulence. The PSDs appear fully turbulent by about $Re_\infty = 4 \times 10^6$/m, as the normalized spectra from both facilities collapse to a common curve above that Reynolds number. However, at lower Re_∞ where the bubble size is larger, small peaks around 20 kHz were observed from both sets of data.

Overall, the results from Figure 14 display excellent agreement between the two conventional-noise hypersonic tunnels. Despite differences in stagnation temperatures, the trends with freestream unit Reynolds number hold across the facilities, supporting any instability analysis derived from each one.

C. Blunt Nosetip

The same analysis was repeated for the blunt, 5 mm nosetip cases. Concatenated schlieren images of the bubble from the AFRL M6LT for three freestream unit Reynolds numbers are displayed in Figure 15 while Figure 16 displays time-averaged schlieren from R2Ch. As observed in Figure 11, the separation bubble is much larger with this nosetip

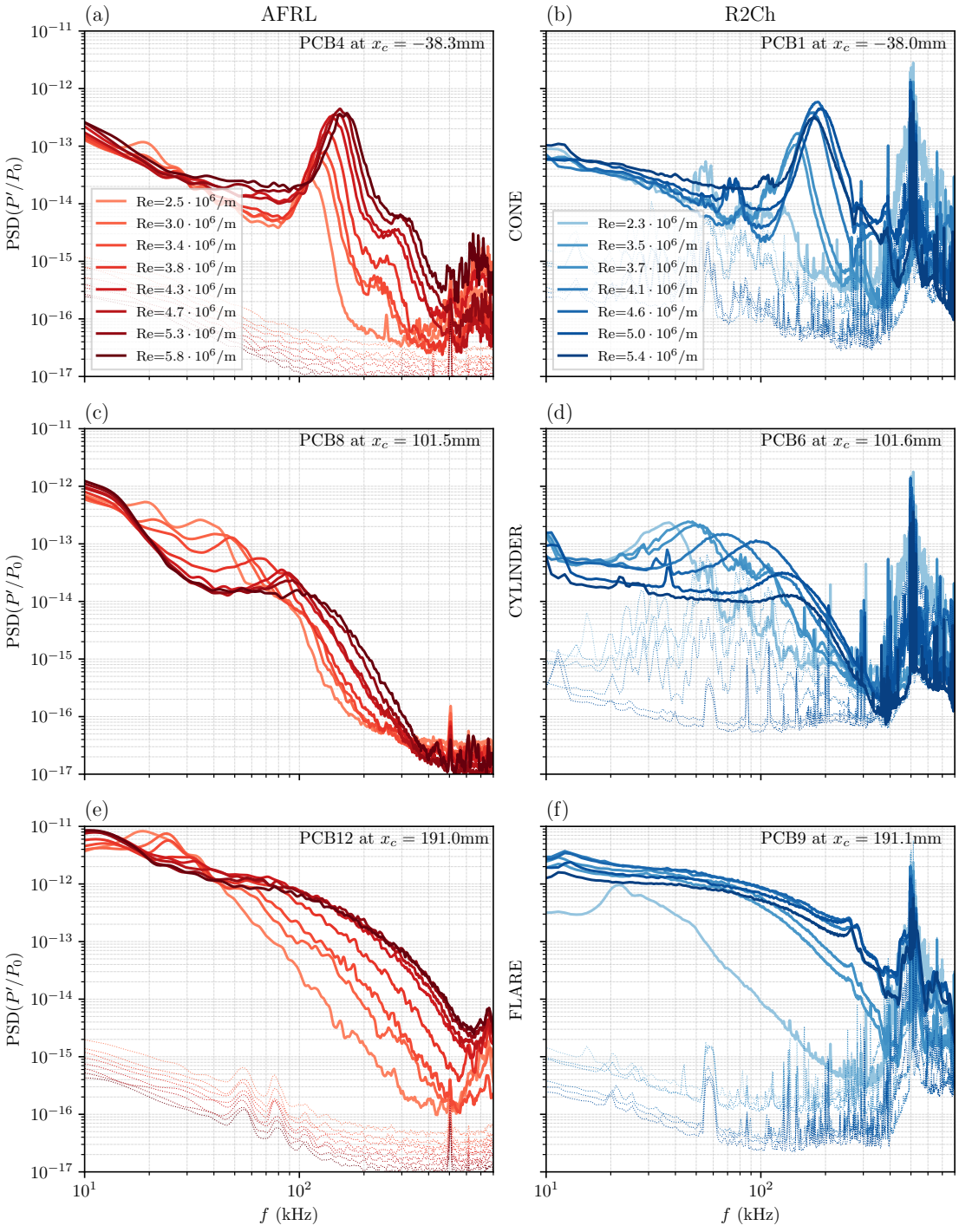

Fig. 14 Comparison of Reynolds number trends along the sharp model for a set of three PCB sensors. Position x_c is given from the cone-cylinder junction.

than the sharp tip at a given freestream Reynolds number. Additionally, different trends between the AFRL and R2Ch facilities were observed for the higher Re_∞ values; in the AFRL M6LT (where the images in Figure 15 were obtained), the bubble size initially increased and then remained constant, while at R2Ch it also initially increased but then began to shrink as Re_∞ increased above 6×10^6/m.

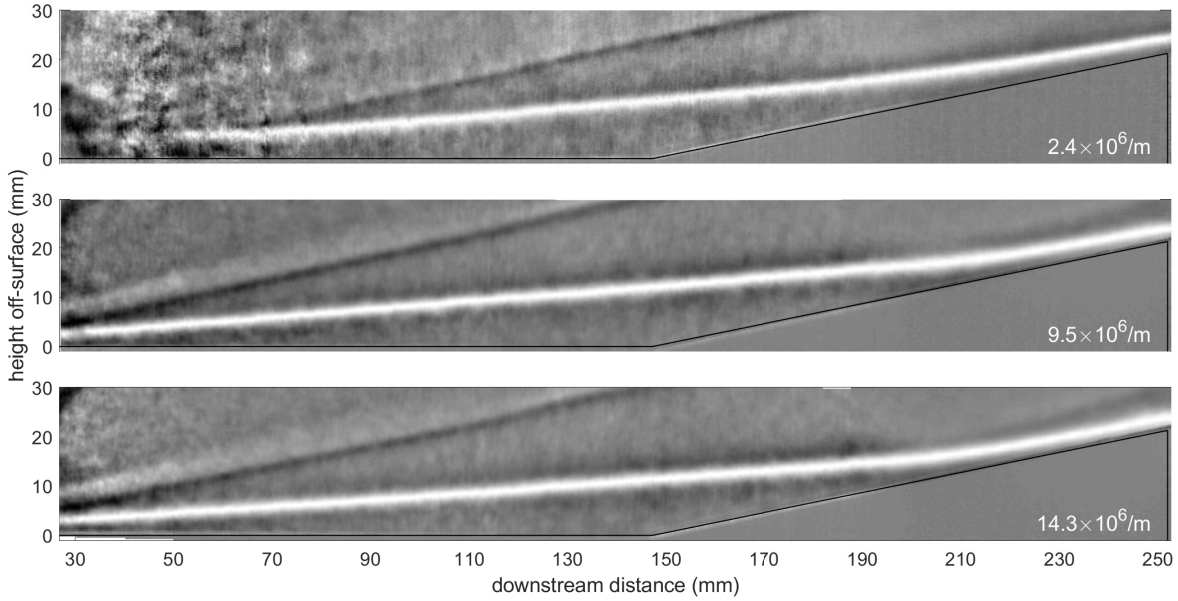

Fig. 15 5 mm nosetip time-averaged and concatenated schlieren imagery from the AFRL M6LT, for Re_∞ = 2.4×10^6/m, 9.5×10^6/m, and 14.3×10^6/m.

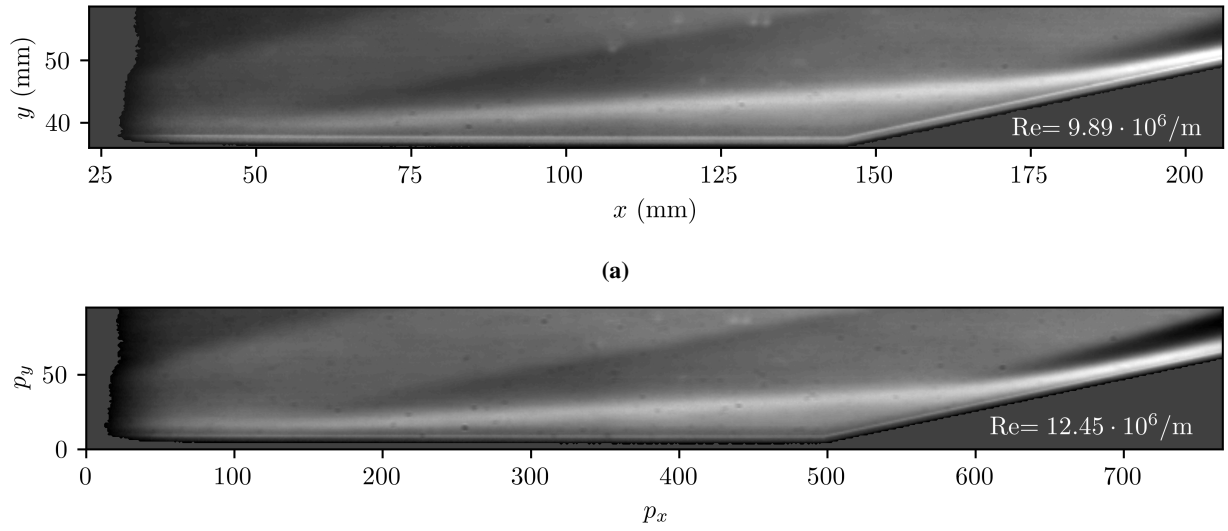

Fig. 16 Blunt nosetip time-averaged schlieren imagery from the R2Ch, for $Re_\infty = 9.9 \times 10^6$/m and 12.45×10^6/m.

PCB power spectral densities are plotted for a station along the cone, cylinder, and flare with the 5 mm nosetip in Figure 17. Along the cone, the second mode appears to be completely damped out, as expected for a blunt cone at zero degrees angle of attack. Both facilities have low-amplitude broadband spectra across the freestream unit Reynolds

numbers tested. The AFRL data, however, do have higher-amplitude values between 10 and 20 kHz relative to the R2Ch data.

Along the cylinder, the spectral differences between the AFRL and R2Ch facilities become more apparent. At AFRL, a slight peak is observed around 15 kHz, along with two other small peaks around 25 and and 50 kHz. These peaks do not vary in peak frequency with changing freestream unit Reynolds number. At R2Ch, however, the 15 kHz peak is not observed, while several large peaks between 30 and 60 kHz and smaller ones between 70 and 100 kHz are seen. These two sets of peaks have a strong correlation with Reynolds number, and increasing in peak frequency with increasing Re_∞.

On the flare, the 15 kHz peak from the AFRL data is even more prominent. There is also a small peak around 30 kHz for the lower freestream Reynolds numbers. From R2Ch, the lower Re_∞ values have peaks between 20 and 30 kHz, while the higher Reynolds numbers have broadband spectra expected for a turbulent boundary layer. It is important to note that at this streamwise position (about 191 mm downstream of the cone-cylinder junction), the AFRL sensor is upstream of reattachment; while in the R2Ch, it is well downstream of the sensor. The variance in positions relative to bubble reattachment could offer a partial explanation for the contrast in spectra along the flare. This still indicates that the flow transition to turbulence at lower Reynolds number in R2Ch compared to M6LT.

The strong difference in flow behavior that was expected from the study of the separation bubble size is confirmed by the spectral data; the R2Ch flow transitions to turbulence while the AFRL the flow remains fully laminar over the whole Reynolds number range.

Three theories that may potentially explain the larger differences between the two facilities for the 5 mm blunt nosetip compared to the sharp nosetip relate to the fundamental differences between the two facilities:

- First, R2Ch is a blowdown tunnel, with an air-heater that continuously heats the air during the run, and both hot (preheated tubing) and cold circuit parts (valves, settling chamber) between the air heater and the nozzle. This leads to a high probability of uneven temperature distribution, and thus, to the presence of numerous entropic spots in the flow (such spots have already been found in similar blowdown tunnels [31]). The M6LT is a Ludwieg tube, which should provide a fully uniform temperature distribution of the air before and during the run, and thus, much less entropic spots in the free-stream. This may be of high importance as blunt flow are known to be prone to entropic instabilities.
- A second hypothesis is linked with the nozzle length of each tunnel. The AFRL M6LT has a nozzle that is significantly longer than the R2Ch Mach-6 nozzle (around 3 times longer). A longer nozzle will result in a thicker boundary layer at the nozzle exit. With a thicker boundary layer, acoustic disturbances introduced into the freestream from boundary-layer turbulence will be of lower frequency as they scale with $\frac{U_e}{\delta}$. Therefore, the AFRL M6LT likely has a freestream noise spectrum that has larger low-frequency disturbances than the R2Ch facility, which likely has larger high-frequency disturbances. This trend should also impact sharp cases and may explain the discrepancies in low frequency spectral content discussed here-before.
- Finally, the stagnation temperature differences between the two facilities may explain the different trends in peak frequencies. If the instabilities observed for the blunt case are entropy-layer instabilities rather than boundary- or shear-layer ones, their peak frequencies are more likely to scale with stagnation temperature rather than Reynolds number. The AFRL M6LT keeps the stagnation temperature relatively constant, which could explain the static PSD peaks at around 15 and 30 kHz. R2Ch, however, generally has a higher stagnation temperature for higher freestream unit Reynolds numbers, potentially resulting in PSD peaks that seem to increase in peak frequency with increasing Re_∞, when they actually are just increasing with increasing T_0.

For the sharp nosetip case, the second mode mechanism has such a significant amplification that even minor disturbances can trigger their growth, resulting in clear second-mode peaks seen from both facilities. Therefore, the sharp case may appear less sensitive to the tunnel noise spectrum. The blunt nosetip case, however, likely has a different dominant instability mechanism, as the second mode is damped out along the cone. This sensitivity would lead to different frequencies being observed in the spectra from AFRL and R2Ch, which can also lead to different bubble sizes due to earlier transition occurring in one facility over the other. This other mechanism may be more sensitive to the freestream noise spectrum, or to the stagnation temperature of the flow. It should be noted that tunnel noise spectra are not currently available for each facility, but the presence of entropic spots in R2Ch as well as the different nozzle lengths leading to different dominant frequency bands of the freestream noise offers two plausible explanations for the differences observed between the two facilities with the blunt nosetip. Additional research is necessary to confirm either hypothesis.

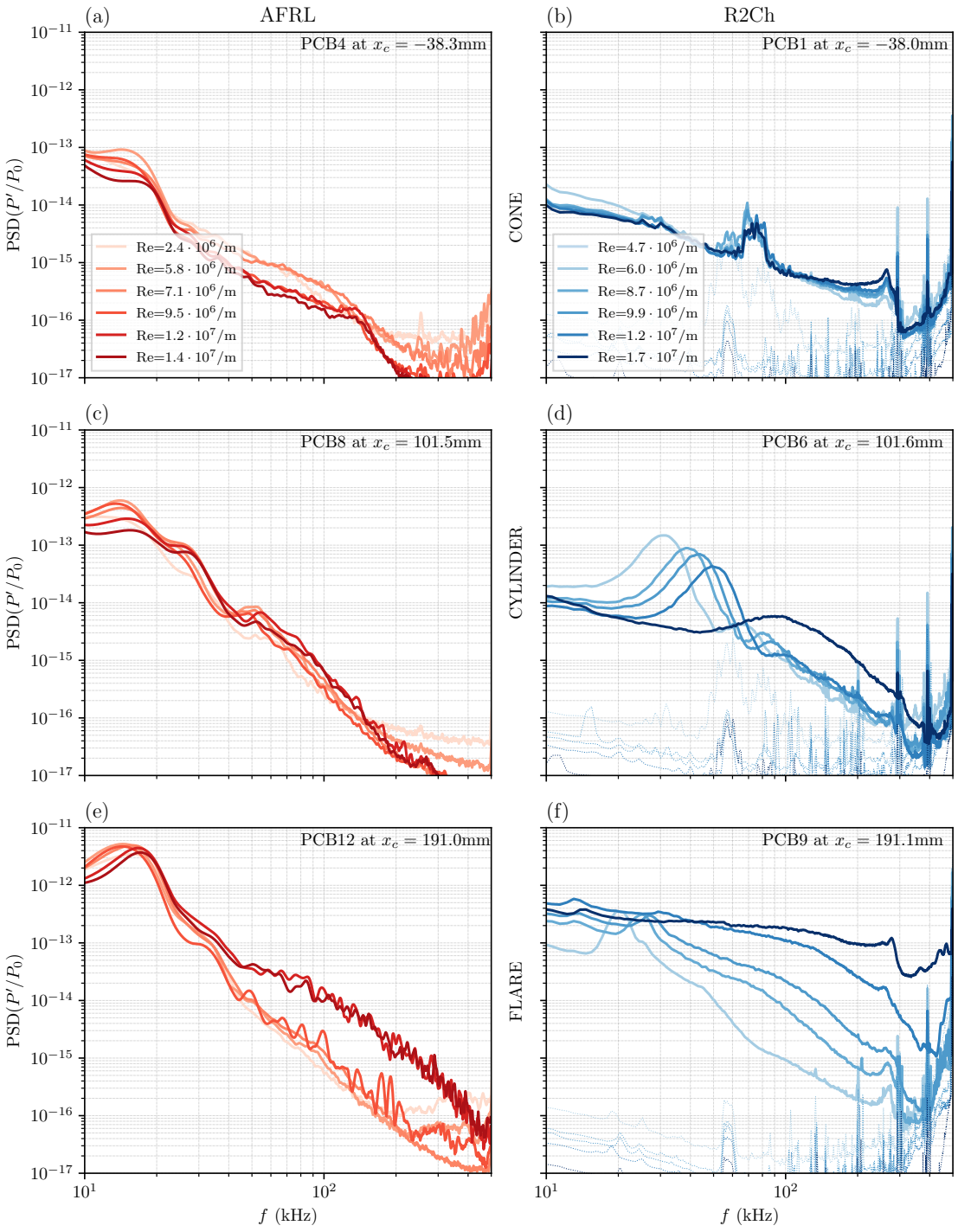

Fig. 17 Comparison of Reynolds number trends along the 5mm model for a set of three PCB sensors. Position x_c is given from the cone-cylinder junction.

V. Selected cases

Two particular cases, one for each of the sharp and 5 mm nosetips, were selected to conduct a more detailed analysis. For the sharp tip, the lowest freestream unit Reynolds number of 2.2×10^6/m was selected, where the flow was mostly laminar. For the 5 mm nosetip, a transitional case at $Re_\infty = 9.9 \times 10^6$/m was chosen.

A. Sharp case at $Re_\infty \approx 2.2 \times 10^6$/m

Figure 18 plots PCB PSDs for sensors on the cone, cylinder, and flare sections at similar locations for the sharp nosetip at $Re_\infty = 2.2 \times 10^6$/m. The results from both the AFRL M6LT and the R2Ch facilities are plotted on the same axes. Excellent agreement is observed between the two tunnels. On the cone, the second mode is clearly seen in each of the spectra peaking around 110 kHz with normalized amplitudes separated by less than a decade. Along the cylinder, a range of first mode peaks are seen in both facilities between 25 and 100 kHz. The normalized amplitudes at the peak varied by less than 20%. The PSDs also include a potential harmonic at about 70 kHz. On the flare, both PSDs have at least one peak at 20 kHz, generally with a broadband falloff above that frequency. This could be a low-pass filtering effect linked with the shock-boundary layer interaction [32]. The normalized peak amplitudes were once again within a decade of each other.

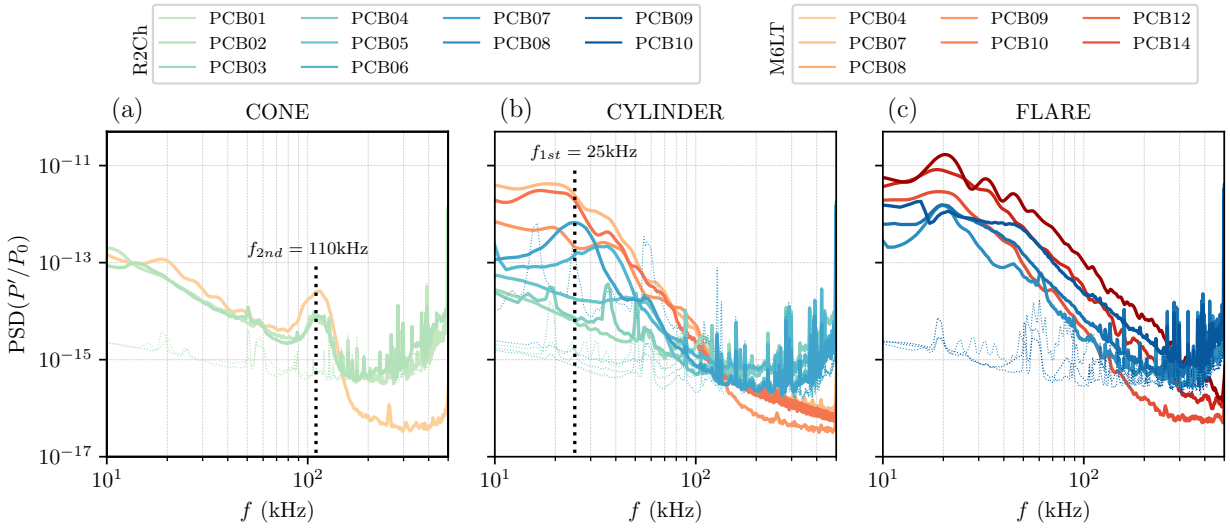

Fig. 18 PCB along the geometry, $Re_\infty = 2.2 \times 10^6$/m.

Additional agreement between the two facilities is observed in the normalized SPOD modal energy, plotted in Figure 19. Albeit not computed on the exact same domain, the first SPOD mode for both tunnels includes a clear peak at around 22 kHz. This disturbance is also visible in the PCB PSD on the flare (Figure 18c) at both facilities, as well as on the cylinder for the AFRL sensor. The leading SPOD disturbance shapes for the 22 kHz mode from each tunnel are displayed in Figure 20. Both disturbances have very similar shapes and sizes, and appear to be amplified moving downstream along the shear layer above the separation bubble.

B. Blunt case at $Re_\infty \approx 9.9 \times 10^6/m$

As noted in Section IV.C, the blunt nosetip power spectral density results did not agree as well as the sharp results across the two facilities. Figure 21 plots PCB PSDs for sensors on the cone, cylinder, and flare sections for the 5 mm nosetip at $Re_\infty = 9.9 \times 10^6$/m. The spectra from the AFRL M6LT and the R2Ch facilities are again overlaid on the same axes. On the cone, the second mode is fully suppressed, with just low levels of broadband fluctuations generally apparent. The exception is for the AFRL results, which have a higher amplitude between 10 and 20 kHz. On the cylinder, the R2Ch spectra include clear peaks between 33 and 65 kHz depending on the sensor. The AFRL PSDs, however, instead have peaks at about 15 kHz. Along the flare, the 15 kHz peak for the AFRL results becomes more prominent with a smaller peak around 33 kHz in some sensors, while the R2Ch results are mostly broadband with a peak at 27 kHz for the upstream-most sensor.

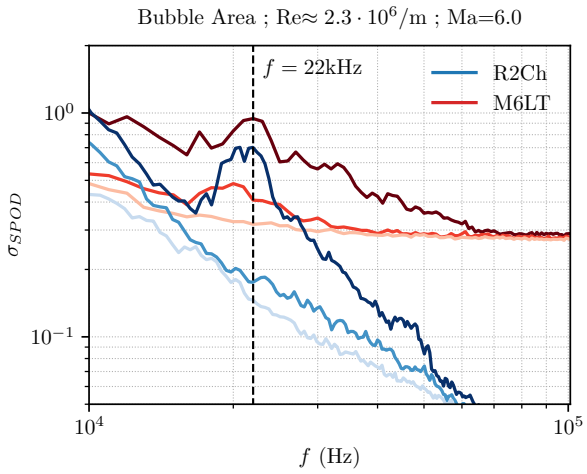

Fig. 19 Normalized SPOD energy around the bubble area for the three first rank at $Re_\infty = 2.2 \times 10^6$/m.

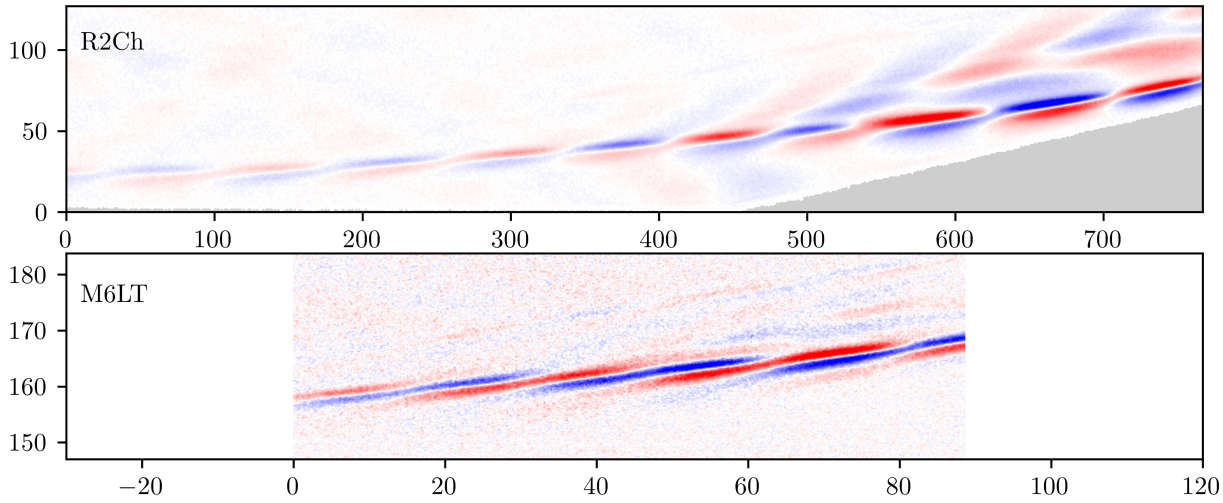

Fig. 20 Leading SPOD mode at the frequency $f = 22kHz$ for case $Re_\infty = 2.2 \times 10^6$/m.

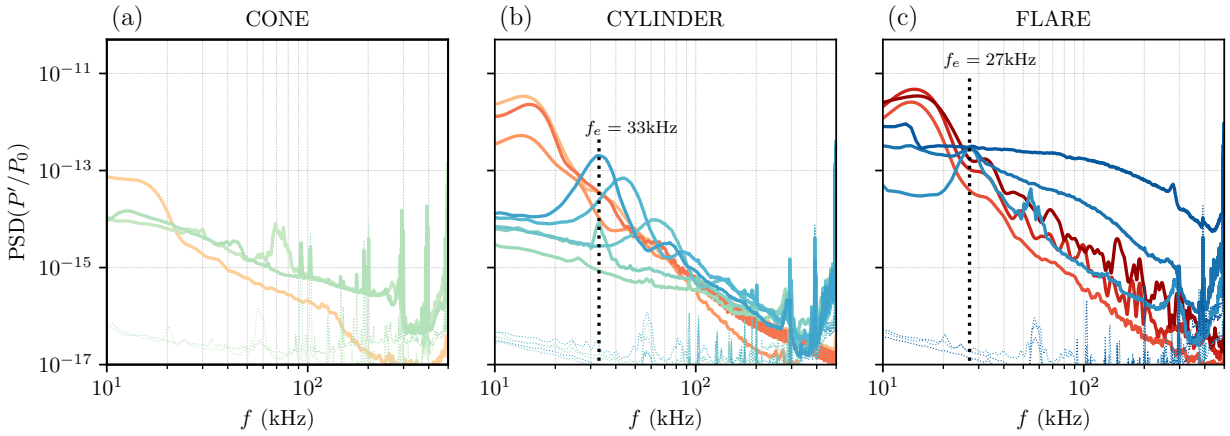

Fig. 21 PCB along geometry, the color code is the same as in Fig. 18, $Re_\infty = 9.9 \times 10^6$/m.

Normalized SPOD modal energies from both facilities are plotted for the blunt nosetip in Figure 22, with the leading SPOD mode shapes displayed in Figure 23. As with the PCB PSDs, the SPOD mode energy plots do not agree between the two tunnels. The first SPOD mode from R2Ch has a clear peak at around 28 kHz. The AFRL data, however, are mostly broadband instead, with relatively higher energy in the 10–30 kHz range for the leading mode. The mode shapes for 28 kHz fluctuations are also very different. At R2Ch, these fluctuations generally first appear around reattachment, while at AFRL, a constant band of elongated structures can be seen across the shear layer. Note again that both the shear layer and reattachment point are present in the R2Ch view, while the AFRL view only contains the bubble and shear layer above it (with a small region of the separation shock in the upper left corner), which could cause different modes to be picked up by the SPOD. For this case, the reattachment region dominated the SPOD results, so the scaling between the two facilities will not be the same due to the exclusion of this region in the AFRL view.

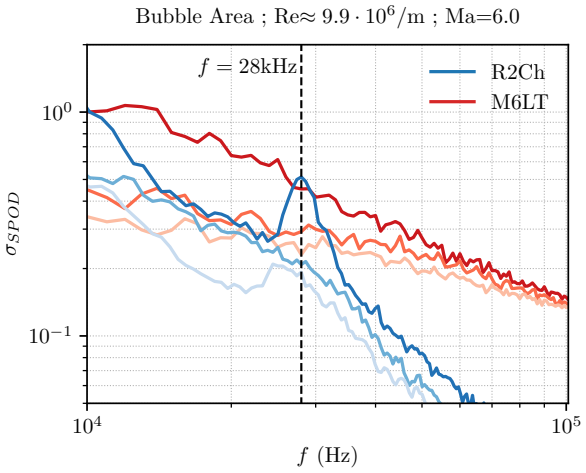

Fig. 22 Normalized SPOD energy around the bubble area for the three first rank at $Re_\infty = 9.9 \times 10^6$/m.

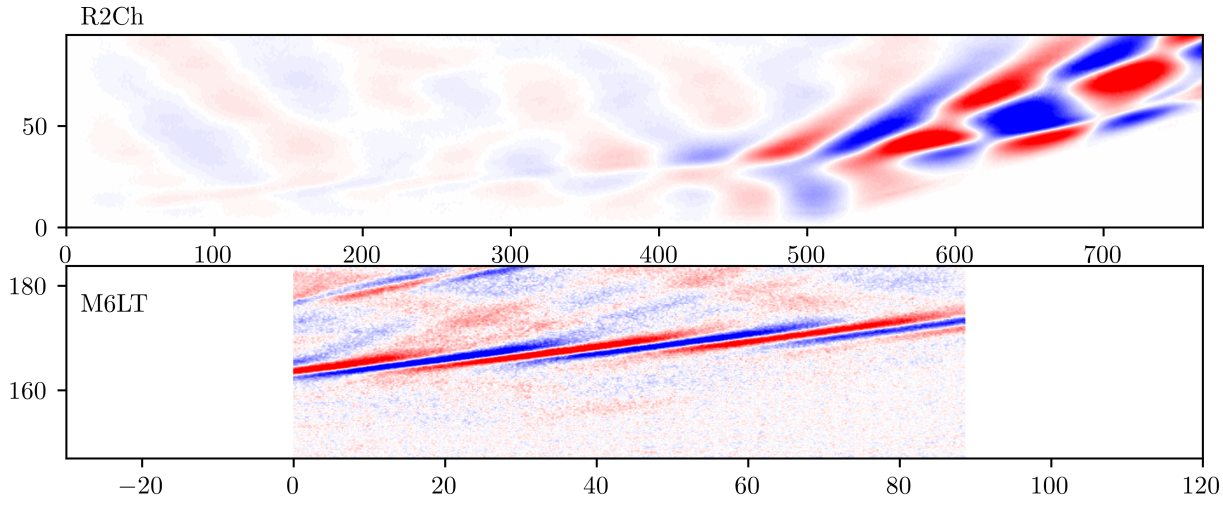

Fig. 23 Leading SPOD mode at the frequency $f = 28kHz$ for R2Ch and $f = 25kHz$ for M6LT at $Re_\infty = 9.9 \times 10^6$/m.

VI. Results under Quiet Flow

Under quiet flow in the BAM6QT, where the freestream disturbance levels are two orders of magnitude below those of conventional hypersonic tunnels but are near the freestream noise levels expected in flight [27, 33, 34], the instability results varied more significantly from those measured at the AFRL M6LT and the R2Ch facilities. Due to the large differences in spectra and transition Reynolds number between the quiet and conventional noise results, the quiet-flow results have been listed separately for clarity. They are important to include, however, due to their more realistic freestream noise levels, which could provide better understanding of receptivity mechanisms that may be present in atmospheric flight.

In the low-disturbance flow, the boundary and shear layers remained laminar to much higher freestream unit Reynolds number, generally resulting in larger separation bubbles at higher Re_∞ compared to the conventional-noise cases for the sharp nosetip. With that tip, no turbulent bursts (fully laminar flow) were observed below freestream unit Reynolds numbers of about 11×10^6/m; the conventional noise facilities, however, observed at least some turbulent bursts at the downstream-most sensors at the lowest Re_∞. Due to these differences in flow state, it is difficult to directly compare the results from the BAM6QT with those from the AFRL M6LT or the R2Ch tunnels. However, it is important to capture the quiet flow results, as they are more likely to include the transition mechanisms present in flight due to their similar freestream noise environments.

Figure 24 plots PCB PSDs along the cone, cylinder, and flare sections of the model with the sharp nosetip under low-disturbance flow. With this tip in quiet flow, the second-mode instability is still measured along the cone. However, its peak frequency is now between 200 and 300 kHz (rather than the 100–200 kHz peaks observed in the conventional facilities) due to the higher freestream unit Reynolds numbers necessary to amplify disturbances in this flow. This change is expected, as the second mode frequency scales with boundary-layer thickness, which itself is a function of freestream Reynolds number. On the cylinder, the peaks dampen out and again shift to a lower peak frequency. Additionally, a second peak can be observed for some Re_∞ values at around 100 kHz. This peak is associated with the shear-layer instability previously observed on the 10° flare under quiet flow. On the flare, both the shear-layer and second-mode instabilities amplify. A nonlinear interaction between the two instabilities is visible for some Re_∞, denoted by a PSD peak with a peak frequency equal to the sum of the peak frequencies of each instability.

Despite the higher transition Reynolds numbers obtained under quiet flow, the same linear transition mechanisms were observed across all three facilities for the sharp nosetip. Both the second mode and shear-layer instabilities were measured in the surface-pressure spectra under both quiet flow and in the conventional hypersonic tunnels, with these convective modes dominating over global modes. This result has been confirmed with numerical study of the same geometry under the same tunnel conditions as those shown here [20].

Due to newly-available higher quiet Reynolds numbers along with a slightly higher flare angle relative to the previously-studied 10° flare, full transition to turbulence with the sharp nosetip under low-disturbance flow was possible to achieve during the BAM6QT experimental campaign for the first time. High Re_∞ runs (above 17×10^6/m) resulted in transitional flow as far upstream as the cone, where second-mode harmonics were measured along with increasing energy in the higher-frequency portion of the spectrum. At these freestream Reynolds levels, the flow transitioned fully by the front of the flare. At a Reynolds number of about $Re_\infty = 14 \times 10^6$/m, turbulent bursts begin to be apparent by the downstream end of the flare, as has been observed in the BAM6QT previously [25]. At an intermediate Reynolds number of $Re_\infty = 16.3 \times 10^6$/m, transition can be observed starting near the beginning of the flare, and achieving the broadband spectrum expected of full turbulence by the end of the flare.

SPOD results from the quiet tunnel support the measurements made with PCBs (Fig. 25). For one run at $Re_\infty = 11.7 \times 10^6$/m, the PCB PSD near the end of the flare has two peaks: one at 110 kHz for the shear-layer instability, and one around 220 kHz for the second mode. In the SPOD mode energy for the second and third SPOD modes, three regions of increased energy appear to be present: one around 110 kHz, one at 221 kHz, and one at 331 kHz. The first two SPOD peaks correspond again to the shear-layer and second-mode instabilities, while the third represents a nonlinear interaction between the two disturbances that has previously been observed in PCB and FLDI bicoherence data for the 10° and 12° flares [24, 35]. This analysis represents the first observation of this interaction via SPOD, where the 331 kHz mode appears as a checkerboard pattern that amplifies moving downstream with a similar wavelength to the shear-layer instability at 110 kHz (Figure 26).

The 5 mm nosetip resulted in very different spectral content. Like in the conventional tunnels, the second mode was suppressed along the cone with the blunter nosetip. However, at the highest freestream unit Reynolds numbers, two small peaks at around the same peak frequencies for the shear-layer instability and the second mode are observable at the end of the cylinder and the beginning of the flare. By the downstream end of the flare, though, only a broadband rise in energy is seen, rather than amplification of the modal peaks.

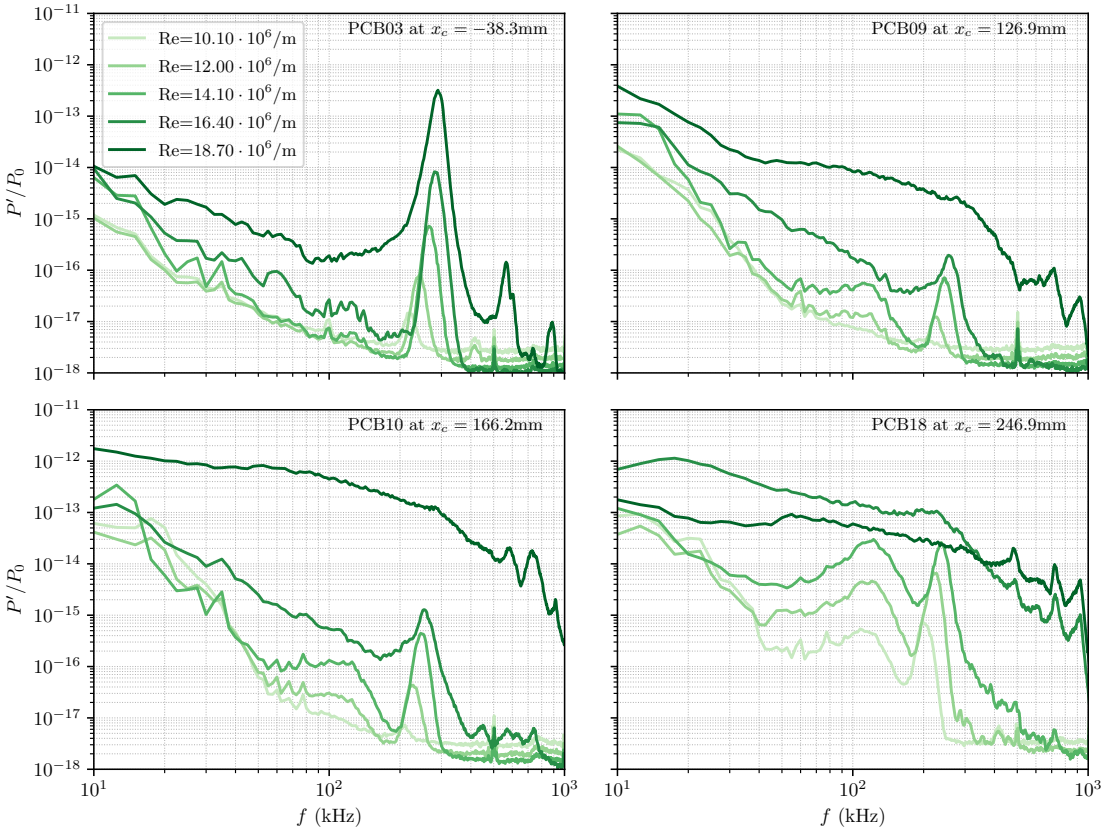

Fig. 24 Reynolds number trends in the BAM6QT along the sharp model for a set of four PCB sensors. Position x_c is given from the cone-cylinder junction. Starting in the upper left corner moving clockwise, sensors are located on the cone, cylinder, upstream flare, and downstream flare.

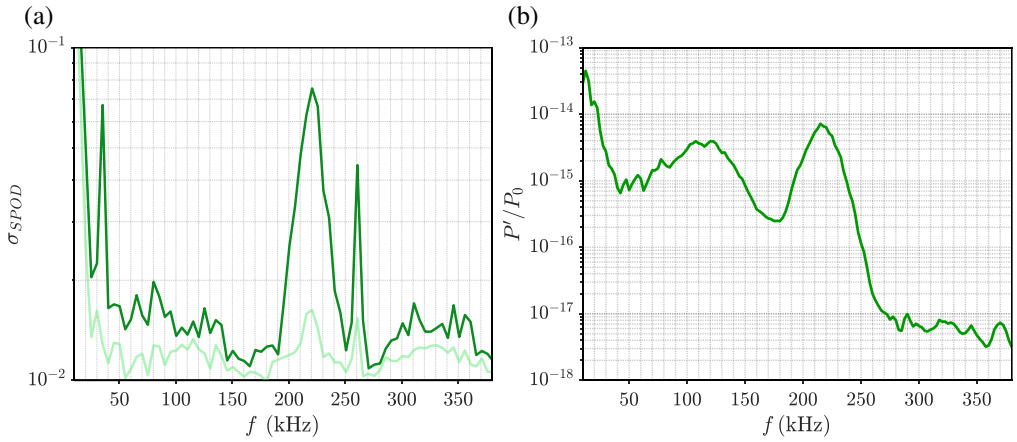

Fig. 25 (a) Normalized SPOD energy around the reattachment area for the second and third SPOD modes at $Re_\infty = 11.7 \times 10^6$/m. (b) PCB 247 mm axially distant from cone-cylinder junction at condition of SPOD in Fig. 26, $Re_\infty = 11.7 \times 10^6$/m.

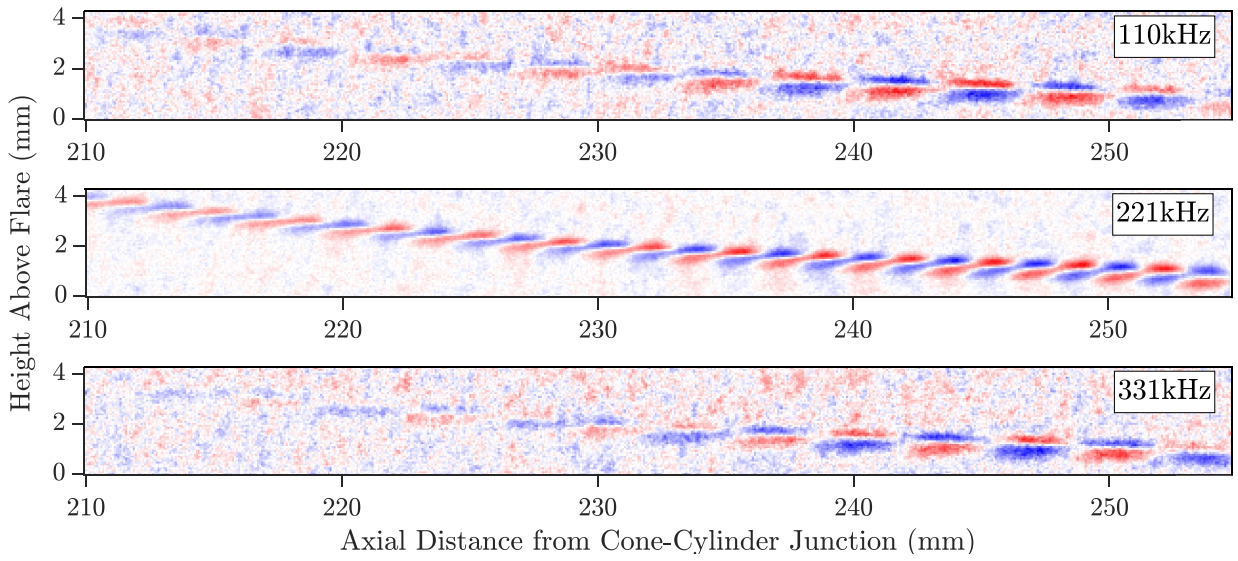

Fig. 26 Second SPOD mode at frequencies corresponding to shear instability, second mode, and addition of both frequencies, $Re_\infty = 11.7 \times 10^6$/m.

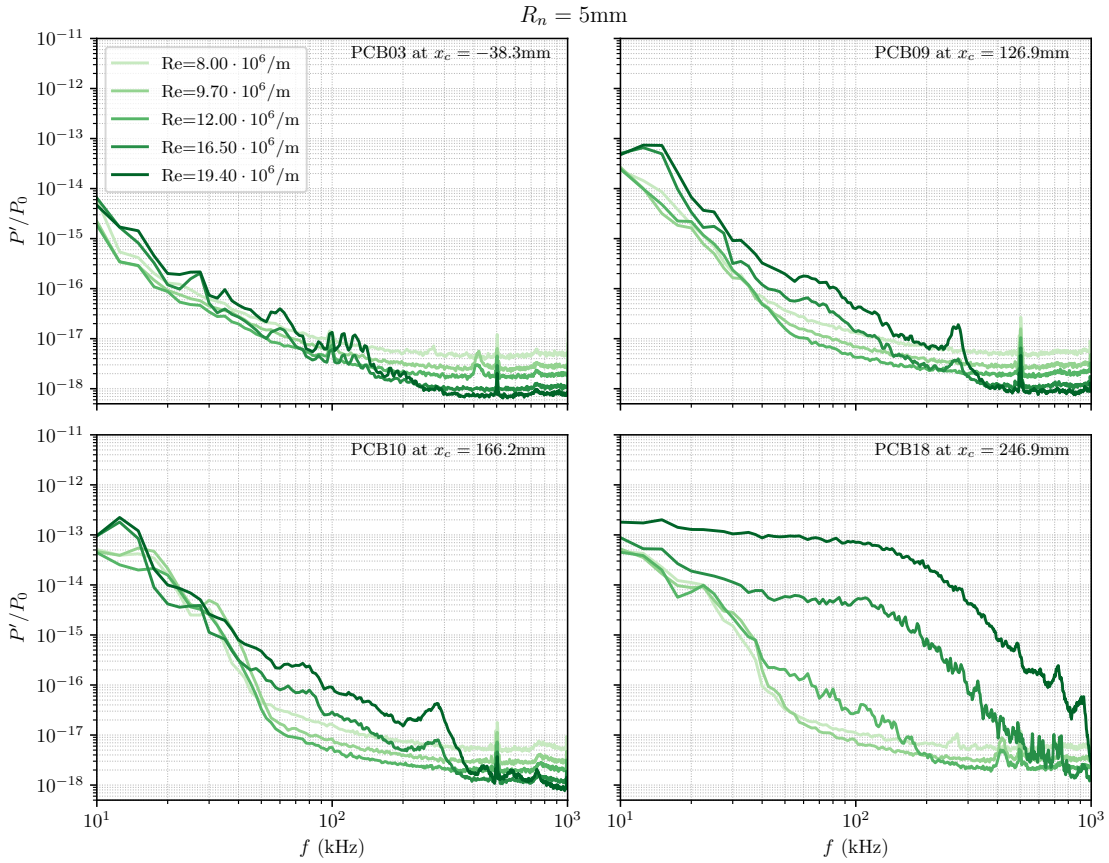

Fig. 27 Reynolds number trends in the BAM6QT along the 5 mm model for a set of four PCB sensors. Position x_c is given from the cone-cylinder junction. Starting in the upper left corner moving clockwise, sensors are located on the cone, cylinder, upstream flare, and downstream flare.

VII. Conclusion

A series of experimental campaigns was undertaken as part of the NATO STO Research Task Group AVT-346 to study the flow instabilities in the presence of an axisymmetric separation bubble over a CCF (CCF) geometry. The experiments took place across three independent facilities and they all involved the measurements of instabilities in a Mach 6 flow over the CCF configuration. Two conventional-noise tunnels, the AFRL M6LT and ONERA R2Ch, along with one quiet-flow tunnel, the Purdue BAM6QT, were used for testing. Two models with an identical geometry were constructed, one for the M6LT and the BAM6QT facilities and the other for the R2Ch. Measurements of surface pressure fluctuation with PCB sensors and off-body flow visualizations with high-speed schlieren imaging were used to study the disturbance characteristics in the attached boundary layer as well as in the shear layer over the separation bubble near the cylinder-flare junction.

Results from the AFRL M6LT and the R2Ch facilities, both conventional-noise hypersonic tunnels, were directly compared. Excellent agreement was observed for the sharp-nose cases across both facilities. With the sharp tip, the flow was generally considered transitional, and the bubble length decreased with an increasing freestream unit Reynolds number, Re_∞. For Re_∞ between 2×10^6/m and 6×10^6/m, the second mode disturbances peaked between 100 kHz and 200 kHz at the PCB on the cone. The disturbances decayed along the expansion fan and the cylinder and their peak frequency also decreased at the same time, but the flow eventually transitioned to a turbulent state near the reattachment location along the flare. PSDs of PCB measurements from both conventional facilities generally aligned in peak frequency for similar conditions, with normalized amplitudes within a decade of each other. The CCF geometry with the blunter, 5 mm nosetip led to greater variance in flow measurements across these two wind tunnels. While the bubble lengths for the sharp nosetip were nearly identical between the two facilities for the entire range of freestream unit Reynolds numbers, the blunt nosetip resulted in different trends, with the separation bubble in the AFRL M6LT generally reattaching downstream of that in the ONERA R2Ch facility as it remained laminar. Differences were also apparent in the PSDs measured by the PCB sensors, with the AFRL tunnel amplifying lower-frequency disturbances relative to the R2Ch tunnel. The main discrepancy being that the flow became turbulent on the flare for moderate to high Reynolds number at R2Ch while it remained fully laminar at M6LT, hinting that there could be important differences in the free-stream noise in both facilities. Three separate hypotheses have been put forward to explain these differences and warrant further examination. These hypotheses include (i) the presence of entropic noise in R2Ch, which should be absent in M6LT, (ii) the difference in acoustic spectra due to the difference in nozzle length, and (iii) the variation in stagnation temperature that could impact the entropy layer supporting the instability.

Results from the BAM6QT, a quiet facility, were described separately due to the significant variation in the state of the flow as well as in the measured instabilities in comparison with the conventional-noise tunnels. Under the low-disturbance flow, both the boundary layer and the shear layer remained fully laminar to much higher freestream unit Reynolds numbers than those in the conventional tunnels. With the sharp nosetip, the second mode peaked between 200 kHz and 300 kHz on the cone and virtually damped out along the cylinder, similar to the conventional faclity measurements. However, two clear peaks were observed along the flare: the second mode gain between 200 kHz and 300 kHz, and the shear-layer instability with a peak frequency of approximately 100 kHz. Due to a higher available quiet Re_∞, full transition was observed along the flare for the first time in a low-disturbance flow. SPOD analysis showed both of these instabilities along the shear layer as well as in the reattached boundary layer downstream, as well as the nonlinear interaction between them. With the 5 mm nosetip, the second mode was damped out along the cone, and a broadband rise in the PSDs of surface pressure fluctuations was observed for the PCB sensors along the flare.

Controlled studies of transition-related phenomena involving the same model geometry in multiple hypersonic ground-test facilities are relatively rare, especially for flows involving separation bubbles due to shock wave/boundary layer interactions. In that regard, the present comparison of experimental results from three different hypersonic wind tunnels on the same CCF geometry is rather significant. As the same geometry was tested under similar conditions in all three facilities, the effects of facility-specific parameters such as freestream noise spectra and stagnation temperatures could be observed. The present study has also revealed the need for additional future work. Specifically, an improved characterization of the freestream noise spectra across the three facilities is necessary to help understand the upstream disturbances in the flow. A follow-on study related to the stagnation temperature variations from the R2Ch would also be beneficial. Finally, the measurements on the blunt-nose CCF configuration in the AFRL M6LT were restricted in their maximum freestream unit Reynolds number due to structural limitations of the model. Manufacturing a stronger model would allow for the full range of the M6LT to be utilized, which could provide further insight into the instability evolution for the higher nose radius.

Additional computational results for this CCF geometry under the same conditions as the experiments described herein are contained in a companion paper by Caillaud et al. [20].

Acknowledgements

The work of the NASA authors (M. Choudhari and F. Li) was supported by the Hypersonic Technology Project (HTP) under the NASA Aeronautics Research Mission Directorate (ARMD). Authors A. Scholten and P. Paredes are supported by the U. S. Office of Naval Research under award number N00014-20-1-2261. Author P. Paredes is also partially supported by the HTP under the NASA ARMD and by the Air Force office of Scientific Research under award number FA9550-20-1-0023. Authors J. Jewell and Z. McDaniel are supported by the U. S. Army under award number W911NF-20-2-0189.

References

[1] Becker, J., and Korycinski, P., "Heat Transfer and Pressure Distribution at a Mach Number of 6.8 on Bodies with Conical Flares and Extensive Flow Separation," Tech. Rep. RM L56F22, NACA, Apr. 1956. DTIC citation AD0274584.

[2] Ginoux, J., "Investigation of Flow Separation over Ramps at M_∞=3," Tech. Rep. AEDC-TR-65-273, Von Karman Gas Dynamics Facility, Arnold Engineering Development Center, Dec. 1965.

[3] Dwivedi, A., Gs, S., Candler, G., Nichols, J., and Jovanovic, M., "Input-Output Analysis of Shock Boundary Layer Interaction," *2018 Fluid Dynamics Conference*, AIAA, Atlanta, GA, 2018. doi:10.2514/6.2018-3220, paper 2018-3220.

[4] Leinemann, M., Radespiel, R., Muñoz, F., Esquieu, S., McKiernan, G., and Schneider, S., "Boundary Layer Transition on a Generic Model of Control Flaps in Hypersonic Flow," *AIAA SciTech 2019 Forum*, AIAA, San Diego, CA, 2019. doi:10.2514/6.2019-1908, paper 2019-1908.

[5] Lugrin, M., Beneddine, S., Leclercq, C., Garnier, E., and Bur, R., "Transition Scenario in Hypersonic Axisymmetrical Compression Ramp Flow," *Journal of Fluid Mechanics*, Vol. 907, 2021, p. A6. doi:10.1017/jfm.2020.833.

[6] Wagner, L., "Amplification of Streamwise Vortices Across a Separated Region at Mach 6," Master's thesis, Purdue University, West Lafayette, Indiana, May 2022.

[7] Inger, G., "Three-Dimensional Disturbances in High Speed Boundary Layer Flows," Tech. Rep. 82-0110, AFOSR, Aug. 1981. DTIC citation ADA120251.

[8] Dolling, D., "Wall Pressure Fluctuations in a Supersonic Separated Compression Ramp Flowfield," *3rd Joint Thermophysics, Fluids, Plasma and Heat Transfer Conference*, AIAA, St. Louis, MO, 1982. doi:10.2514/6.1982-986, URL `http://arc.aiaa.org/doi/10.2514/6.1982-986`, paper 82-0986.

[9] Oberkampf, W., and Aeschliman, D., "Joint Computational/Experimental Aerodynamics Research on a Hypersonic Vehicle, Part I: Experimental Results," *AIAA Journal*, Vol. 30, No. 8, 1992, pp. 2000–2009. doi:10.2514/3.11172.

[10] McKiernan, G., "Instability of the Shear Layer on a Sliced Cone with Finite Span Compression Ramps at Mach 6," Ph.D. thesis, Purdue University, West Lafayette, Indiana, May 2020.

[11] Benitez, E., Jewell, J., Schneider, S., and Esquieu, S., "Instability Measurements on an Axisymmetric Separation Bubble at Mach 6," *AIAA Aviation 2020 Forum*, AIAA, Virtual, 2020. doi:10.2414/6.2020-3072, paper 2020-3072.

[12] Lugrin, M., Nicolas, F., Severac, N., Tobeli, J., Beneddine, S., Garnier, E., Esquieu, S., and Bur, R., "Transitional Shockwave/Boundary Layer Interaction Experiments in the R2Ch Blowdown Wind Tunnel," *Experiments in Fluids*, Vol. 63, No. 46, 2022. doi:10.1017/jfm.2020.833.

[13] Butler, C., and Laurence, S., "Transitional Hypersonic Flow over Slender Cone/Flare Geometries," *Journal of Fluid Mechanics*, Vol. 949, 2022. doi:10.1017/jfm.2022.769.

[14] Esquieu, S., Benitez, E., Schneider, S., and Brazier, J., "Flow and Stability Analysis of a Hypersonic Boundary-Layer over an Axisymmetric Cone-Cylinder-Flare Configuration," *AIAA SciTech 2019 Forum*, AIAA, San Diego, CA, 2019. doi:10.2514/6.2019-2115, paper 2019-2115.

[15] Esquieu, S., Schneider, S., Benitez, E., and Brazier, J., "Design of a Cone-Cylinder-Flare Configuration for Hypersonic Boundary-Layer Stability Analyses and Measurements with Attached and Separated Flows," *AERO 2023-The 3AF International Conference on Applied Aerodynamics*, Bordeaux, France, 2023.

[16] Benitez, E., Jewell, J., and Schneider, S., "Separation Bubble Variation Due to Small Angles of Attack for an Axisymmetric Model at Mach 6," *AIAA SciTech 2021 Forum*, AIAA, Virtual, 2021. doi:10.2414/6.2021-0245, paper 2021-0245.

[17] Benitez, E., Jewell, J., and Schneider, S., "Propagation of Controlled Disturbances through an Axisymmetric Separation Bubble at Mach 6," *AIAA Aviation 2021 Forum*, AIAA, Virtual, 2021. doi:10.2414/6.2021-2844, paper 2021-2844.

[18] Benitez, E., Borg, M., Paredes, P., Schneider, S., and Jewell, J., "Measurements of an Axisymmetric Hypersonic Shear-Layer Instability in Quiet Flow," *Physical Review Fluids*, Vol. 8, No. 8, 2023, p. 083903. doi:10.1103/PhysRevFluids.8.083903.

[19] Paredes, P., Scholten, A., Choudhari, M., Li, F., Benitez, E., and Jewell, J., "Boundary-Layer Instabilities Over a Cone-Cylinder-Flare Model at Mach 6," *AIAA SciTech 2022 Forum*, AIAA, San Diego, CA, 2022. doi:10.2514/6.2022-0600, paper 2022-0600.

[20] Caillaud, C., Lugrin, M., Esquieu, S., Scholten, A., Paredes, P., Choudhari, M., Li, F., Benitez, E., Borg, M., McDaniel, Z., and Jewell, J., "Separation and Transitionon a Cone-Cylinder-Flare: Computational Analysis," *AIAA SciTech 2024 Forum*, AIAA, Orlando, FL, 2024. To be presented.

[21] Benitez, E., "Instability Measurements on Two Cone-Cylinder-Flares at Mach 6," Ph.D. thesis, Purdue University, West Lafayette, Indiana, 2021. doi:10.25394/PGS.15050058.v1.

[22] Paredes, P., Scholten, A., Choudhari, M., Li, F., Benitez, E., and Jewell, J., "Boundary-Layer Instabilities Over a Cone-Cylinder-Flare Model at Mach 6," *AIAA Journal*, Vol. 60, No. 10, 2022. doi:10.2514/1.J061829.

[23] Benitez, E., Borg, M., Hill, J., Scholten, A., Paredes, P., and Jewell, J., "Measurements on a Blunt Cone-Cylinder-Flare at Mach 6," *AIAA SciTech 2023 Forum*, AIAA, National Harbor, MD, 2023. doi:10.2514/6.2023-1245, paper 2023-1245.

[24] Benitez, E., Borg, M., McDaniel, Z., and Jewell, J., "Instability and Transition Onset Downstream of an Axisymmetric Separation Bubble with Sharp and Blunt Nosetips," *AIAA Aviation 2023 Forum*, AIAA, San Diego, CA, 2023. doi:10.2514/6.2023-3702, paper 2023-3702.

[25] Benitez, E., Borg, M., Scholten, A., Paredes, P., McDaniel, Z., and Jewell, J., "Instability and Transition Onset Downstream of a Laminar Separation Bubble at Mach 6," *Journal of Fluid Mechanics*, Vol. 969, 2023, p. A11. doi:10.1017/jfm.2023.533.

[26] Kimmel, R., Borg, M., Jewell, J., Lam, K., Bowersox, R., Srinivasan, R., Fuchs, S., and Mooney, T., "AFRL Ludwieg Tube Initial Performance," *55th AIAA Aerospace Sciences Meeting*, AIAA, Grapevine, TX, 2017. doi:10.2514/6.2017-0102, URL https://arc.aiaa.org/doi/abs/10.2514/6.2017-0102, paper 2017-0102.

[27] Schneider, S., "Development of Hypersonic Quiet Tunnels," *Journal of Spacecraft and Rockets*, Vol. 45, No. 4, 2008, p. 641–664. doi:10.2514/1.34489.

[28] Towne, A., Schmidt, O., and Colonius, T., "Spectral Proper Orthogonal Decomposition and its Relationship to Dynamic Mode Decomposition and Resolvent Analysis," *Journal of Fluid Mechanics*, Vol. 847, 2018, p. 821–867. doi:10.1017/jfm.2018.283.

[29] Schmidt, O., and Colonius, T., "Guide to Spectral Proper Orthogonal Decomposition," *AIAA Journal*, Vol. 58, No. 3, 2020, pp. 1023–1033. doi:10.2514/1.J058809.

[30] Marxen, O., and Rist, U., "Mean Flow Deformation in a Laminar Separation Bubble: Separation and Stability Characteristics," *Journal of Fluid Mechanics*, Vol. 660, 2010, pp. 37–54.

[31] Masutti, D., Spinosa, E., Chazot, O., and Carbonaro, M., "Disturbance level characterization of a hypersonic blowdown facility," *AIAA journal*, Vol. 50, No. 12, 2012, pp. 2720–2730.

[32] Touber, E., and Sandham, N., "Large-Eddy Simulation of Low-Frequency Unsteadiness in a Turbulent Shock-Induced Separation Bubble," *Theoretical and Computational Fluid Dynamics*, Vol. 23, No. 2, 2009, pp. 79–107. doi:10.1007/s00162-009-0103-z.

[33] Juliano, T., Swanson, E., and Schneider, S., "Transition Research and Improved Performance in the Boeing/AFOSR Mach-6 Quiet Tunnel," *45th AIAA Aerospace Sciences Meeting and Exhibit*, AIAA, Reno, NV, 2007. doi:10.2514/6.2007-535, paper 2007-535.

[34] Schneider, S., "Developing mechanism-based methods for estimating hypersonic boundary-layer transition in flight: The role of quiet tunnels," *Journal of Spacecraft and Rockets*, Vol. 72, No. 4, 2015, p. 17–29. doi:10.1016/j.paerosci.2014.09.008.

[35] Benitez, E., Leger, T., Tufts, M., Borg, M., and Hill, J., "Hypersonic Transitional Boundary-Layer Profile using a Linear-Array FLDI," *AIAA Aviation 2023 Forum*, AIAA, San Diego, CA, 2023. doi:10.2514/6.2023-4253, paper 2023-4253.